

## Structural densification of lithium phosphoaluminoborate glasses

Liu, Pengfei; Søndergaard, Andreas L.S.; Youngman, Randall E.; Rzoska, Sylwester J.; Bockowski, Michał; Jensen, Lars R.; Smedskjaer, Morten M.

*Published in:*  
Journal of the American Ceramic Society

*DOI (link to publication from Publisher):*  
[10.1111/jace.17559](https://doi.org/10.1111/jace.17559)

*Creative Commons License*  
CC BY-NC 4.0

*Publication date:*  
2021

*Document Version*  
Accepted author manuscript, peer reviewed version

[Link to publication from Aalborg University](#)

*Citation for published version (APA):*  
Liu, P., Søndergaard, A. L. S., Youngman, R. E., Rzoska, S. J., Bockowski, M., Jensen, L. R., & Smedskjaer, M. (2021). Structural densification of lithium phosphoaluminoborate glasses. *Journal of the American Ceramic Society*, 104(3), 1345–1359. <https://doi.org/10.1111/jace.17559>

### General rights

Copyright and moral rights for the publications made accessible in the public portal are retained by the authors and/or other copyright owners and it is a condition of accessing publications that users recognise and abide by the legal requirements associated with these rights.

- Users may download and print one copy of any publication from the public portal for the purpose of private study or research.
- You may not further distribute the material or use it for any profit-making activity or commercial gain
- You may freely distribute the URL identifying the publication in the public portal -

### Take down policy

If you believe that this document breaches copyright please contact us at [vbn@aub.aau.dk](mailto:vbn@aub.aau.dk) providing details, and we will remove access to the work immediately and investigate your claim.

MR. PENGFEI LIU (Orcid ID : 0000-0003-2885-4721)

DR MORTEN SMEDSKJAER (Orcid ID : 0000-0003-0476-2021)

Article type : Article

## Structural Densification of Lithium Phosphoaluminoborate Glasses

Pengfei Liu<sup>1</sup>, Andreas L. S. Søndergaard<sup>1</sup>, Randall E. Youngman<sup>2</sup>, Sylwester J. Rzoska<sup>3</sup>, Michal Bockowski<sup>3</sup>, Lars R. Jensen<sup>4</sup>, Morten M. Smedskjaer<sup>1,\*</sup>

<sup>1</sup>*Department of Chemistry and Bioscience, Aalborg University, Aalborg, Denmark*

<sup>2</sup>*Science and Technology Division, Corning Incorporated, Corning, USA*

<sup>3</sup>*Institute of High-Pressure Physics, Polish Academy of Sciences, Warsaw, Poland*

<sup>4</sup>*Department of Materials and Production, Aalborg University, Aalborg, Denmark*

\*Corresponding author. e-mail: mos@bio.aau.dk

**Abstract:** Lithium aluminoborate glasses have recently been found to undergo dramatic changes in their short-range structures upon compression at moderate pressure (~1 GPa), most notably manifested in an increase in network forming cation coordination number. This has important consequences for their mechanical behavior and to further understand the structural densification mechanisms of this glass family, we here study the effect of P<sub>2</sub>O<sub>5</sub> incorporation in a lithium aluminoborate glass (with fixed Li/Al/B ratio) on the pressure-induced changes in structure, density, and hardness. We find that P<sub>2</sub>O<sub>5</sub> addition results in a more open and soft network, with P-O-Al and P-O-B bonding, a slightly smaller fraction of tetrahedral-to-trigonal boron, and an unchanged aluminum speciation. Upon compression, the cation-oxygen coordination numbers (CNs) of both boron and aluminum increase systemically, whereas the number of bridging oxygens around phosphorous ( $Q^n$ ) decreases. The glasses with higher P<sub>2</sub>O<sub>5</sub> content feature a larger decrease

This article has been accepted for publication and undergone full peer review but has not been through the copyediting, typesetting, pagination and proofreading process, which may lead to differences between this version and the [Version of Record](#). Please cite this article as [doi: 10.1111/JACE.17559](https://doi.org/10.1111/JACE.17559)

This article is protected by copyright. All rights reserved

Accepted Article

in  $Q''$  (P) upon compression, which leads to more non-bridging oxygens that in turn fuel the larger increase in CN of B and Al for higher  $P_2O_5$  content. We find that the CN changes of Al and B can account for a large fraction (around 50% at 2 GPa) of the total volume densification and that the extent of structural changes (so-called atomic self-adaptivity) scales well with the extent of volume densification and pressure-induced increase in hardness.

## 1. Introduction

Oxide glasses play a critical role for innovation in a range of industries due to their combination of favorable properties such as transparency, high hardness, relatively light weight, and chemical durability<sup>1</sup>. Although the ultimate strength and ductility of defect-free amorphous oxides can be high<sup>2,3</sup>, bulk oxide glasses generally possess low fracture toughness (around 0.5 to 1.0 MPa m<sup>0.5</sup>) because of the lack of a stable shearing deformation mechanism and limited resistance to crack growth<sup>4,5,6</sup>. In the past few decades, scientists have made great efforts to improve the mechanical reliability and resistance to surface damage of glasses through effective surface treatments, among which thermal tempering<sup>7</sup> and chemical strengthening<sup>8,9</sup> are the most widespread, with the aim to improve strength and increase the critical stress needed for crack initiation. In addition to adding extra cost, these methods are also limited to either relatively thick glasses (thermal tempering) or mobile ion-containing glasses (chemical strengthening).

A key consideration when designing new damage resistant glasses is their densification mechanism under high pressure<sup>10</sup>. Moreover, compression treatments could potentially provide an additional degree of freedom to balance different properties in the composition-temperature-pressure plane. The change in glass properties under an applied pressure is related to the extent of volume densification and corresponding structural changes at both short- and intermediate-range length scales<sup>11</sup>. Although oxide glasses are macroscopically brittle, they undergo plastic deformation under high stresses, e.g., during indentation<sup>12</sup>. By studying different glass compositions, Peter showed that the indentation deformation mechanism of oxide glasses in general includes both shear flow and densification<sup>13</sup>, with the simple notion that shear flow is the dominant process for glasses with compact structures, whereas densification becomes increasingly important in more open glasses<sup>14,15</sup>. Densification causes volume shrinkage, but can be recovered upon sub- $T_g$  (where  $T_g$  is the glass transition temperature) annealing<sup>15,16</sup>. In turn, pre-densification of a glass affects the deformation mechanism during subsequent indentation as well as other mechanical properties. For example, Svenson et al.<sup>17</sup> found that the pressure-induced changes in elastic moduli are not governed by the specific structural changes, but rather by the overall degree of network densification. Deschamps et al.<sup>18</sup> found that the variation in the elastic moduli is also dependent on the compression path taken to reach permanent densification. Hardness is also affected by densification, since it is sensitive to the local bonding and atomic packing behavior of the constituent atoms and presence of, e.g., non-bridging oxygens (NBOs)<sup>19</sup>. In general, hardness increases with density and Kapoor et al.<sup>20</sup> found that an overall network densification is responsible for this increase. Furthermore, Smedskjaer et al.<sup>21</sup> found that the changes in hardness also depends on the compression path taken to reach permanent densification, such as annealing versus hot compression. Despite the importance of volume densification, the structural changes such as increasing network-former coordination numbers (e.g., for B and Al) upon densification<sup>22</sup> need to be considered for properties such as crack initiation resistance<sup>23,24,25,19</sup>.



In this work, we build on previous studies in understanding structural densification mechanisms in alkali aluminoborate glasses<sup>26,27,28</sup>. These glasses generally exhibit high crack initiation resistance upon indentation, including for a lithium aluminoborate glass<sup>23</sup> that shows a dramatic increase in the coordination numbers of both boron and aluminum upon high-temperature densification. In a recent work, we studied the effect of adding SiO<sub>2</sub> (up to 20 mol%) to a 25Li<sub>2</sub>O-20Al<sub>2</sub>O<sub>3</sub>-55B<sub>2</sub>O<sub>3</sub> glass on the structure and mechanical properties<sup>29</sup>. Addition of silica increases the average network rigidity, but meanwhile its open tetrahedral structure decreases the atomic packing density and also makes the network less structurally-adaptive to applied stress. This is because Al and B easily increase their coordination number under pressure, while this is not the case for Si under modest pressures. As such, although the silica-containing networks have more free volume, they cannot densify more during indentation, which in turn leads to an overall decrease in crack resistance upon SiO<sub>2</sub> addition. In a related work<sup>30</sup>, Dickinson and de Jong found an increase in the boron coordination number upon P<sub>2</sub>O<sub>5</sub> addition in borosilicate glass. Previous studies<sup>31,24</sup> have shown that the presence of B<sup>IV</sup> relative to B<sup>III</sup> units decreases the extent of volume densification in borosilicate glasses due to a more open network and planar structure of the latter.

To further understand the structural densification behavior of this glass family, we here study the effect of P<sub>2</sub>O<sub>5</sub> addition (up to 10 mol%) to a 25Li<sub>2</sub>O-20Al<sub>2</sub>O<sub>3</sub>-55B<sub>2</sub>O<sub>3</sub> glass on the pressure-induced changes in glass structure using Raman, NMR spectroscopy, density measurements, indentation hardness testing, and ultrasonic echography. We refer to these glasses as lithium phosphoaluminoborate glasses, since B<sub>2</sub>O<sub>3</sub> remains the major network-forming oxide. In this glass series, we keep the Li/Al/B ratio constant. This is done to keep the structural role of Al unchanged, which is expected to be possible because it has a strong enthalpic preference for being charge-stabilized by alkali cations (e.g., Li<sup>+</sup>) in tetrahedral configuration<sup>23</sup>.

## 2. Experimental

### 2.1 Glass preparation

Lithium phosphoaluminoborate glasses,  $x\text{P}_2\text{O}_5-(1-x)[25\text{Li}_2\text{O}-20\text{Al}_2\text{O}_3-55\text{B}_2\text{O}_3]$  with  $x = \{0, 2, 5, 10\}$  (in mol%), were synthesized using the traditional melt-quenching approach. The utilized raw materials were Li<sub>2</sub>CO<sub>3</sub> ( $\geq 98.5\%$ , Merck KGaA), Al<sub>2</sub>O<sub>3</sub> (99.5%, Sigma-Aldrich), H<sub>3</sub>BO<sub>3</sub> ( $\geq 99.5\%$ , Honeywell International), and NH<sub>4</sub>PO<sub>4</sub> ( $\geq 99.5\%$ , Merck KGaA). First, according to the target composition, all raw materials were weighed and thoroughly mixed. In order to prevent excessive foaming, the mixed powders were stepwise added to a 100 mL alumina crucible and heated to around 500 °C in an electric furnace (Entech) to remove the excess H<sub>2</sub>O, CO<sub>2</sub>, and NH<sub>3</sub>. The mixture was melted and homogenized at 1150-1250 °C for 1 h in air. Then the melt was poured onto a brass plate for quenching. Finally, the obtained glasses were immediately transferred to a preheated annealing furnace at an estimated glass transition

temperature ( $T_g$ ) value for 30 min, and then slowly cooled down to room temperature. The chemical compositions of the glasses were analyzed using inductively coupled plasma optical emission spectroscopy for  $P_2O_5$ ,  $Al_2O_3$  and  $B_2O_3$ , and flame emission spectroscopy for determination of  $Li_2O$  content (see Table 1). Furthermore, as shown in Figure S1 in the Supporting Information, x-ray diffraction analysis indicated that none of the samples showed any signs of crystallization.

We determined  $T_g$  of the glasses using differential scanning calorimetry (STA 449 F3 Jupiter, Netzsch). The measurements were done at 10 K/min on specimens with a known thermal history (i.e., with a preceding cooling rate of 10 K/min) using Pt crucible in argon (gas flow 60 mL/min).  $T_g$  values and other property data are summarized in Table S1 in the Supporting Information. Following determination of  $T_g$ , the glasses were re-annealed for 30 min at their measured  $T_g$  value and cooled down to room temperature at a cooling rate of approximately 3 K/min. After re-annealing, all the glasses were cut into desired dimensions and optically polished in ethanol by using SiC grinding paper ranging from grit 220 to 4000 in 6 steps.

## 2.2 Hot compression

Following the method described in the previous study<sup>32</sup>, all four annealed glasses were subjected to an isostatic  $N_2$ -mediated pressure treatment at both 1 and 2 GPa. The compression was carried out at the measured ambient-pressure  $T_g$  value for 30 min. The samples were subsequently quenched at an initial cooling rate of 60 K/min. The pressure chamber was then decompressed at a rate of 30 MPa/min at room temperature.

## 2.3 Density

Density ( $\rho$ ) of the glass specimens was determined using Archimedes' principle of buoyancy. The weight of each specimen (at least 1.5 g) was measured in air and ethanol ten times. Based on the ratio between molar mass and density, we calculate the molar volume ( $V_m$ ). To also quantify differences in free volume among the different glasses, we calculate the atomic packing density ( $C_g$ ) based on these data. This was done by assuming 6-fold coordination for Li, 2-fold coordination for O, while the coordination number for B and Al are taken from the NMR results.  $C_g$  is defined as the ratio between the theoretical molar volume occupied by the ions and the effective molar volume of the glass,

$$C_g = \rho \frac{\sum f_i V_i}{\sum f_i M_i} \quad (1)$$

Here,  $V_i = \frac{4}{3}\pi N (x r_A^3 + y r_B^3)$  represents the molar volume of an oxide  $A_x B_y$  with the molar fraction  $f_i$  and the molar mass  $M_i$ ,  $N$  denotes Avogadro's number, and  $r_A$  and  $r_B$  of are the ionic radii of the cations and anions, respectively, which are taken from Shannon<sup>33</sup>.

## 2.4 Raman spectroscopy

To study the short- and intermediate-range structural changes due to composition variation and hot compression, we have acquired micro-Raman spectra of the glasses. The spectra were collected on an inVia micro-Raman spectrometer (Renishaw). All samples surfaces were excited by a 532 nm green diode laser for an acquisition time of 10 s. The range of all spectra was from 220 to 1700  $\text{cm}^{-1}$ , with resolution better than 2  $\text{cm}^{-1}$ . Spectra from three different locations on the glass were compared for each specimen to verify chemical homogeneity (see Figure S2 in the Supporting Information). All spectra were uniformly treated in Origin software for background correction and area normalization.

## 2.5 Solid state NMR spectroscopy

$^{11}\text{B}$  and  $^{27}\text{Al}$  magic-angle spinning nuclear magnetic resonance (MAS NMR) experiments were conducted at 16.4 T by using a commercial spectrometer (VNMRS, Agilent) and a commercial 3.2 mm MAS NMR probe (Agilent). Resonance frequencies for  $^{11}\text{B}$  and  $^{27}\text{Al}$  at this external magnetic field were 224.52 and 182.34 MHz, respectively. Glasses were powdered with an agate mortar and pestle, and then loaded into low-Al zirconia rotors for sample spinning at 20 and 22 kHz for  $^{11}\text{B}$  and  $^{27}\text{Al}$  MAS NMR. Data for both nuclei were collected with short radio-frequency pulse widths of 0.6  $\mu\text{s}$  ( $\pi/12$  tip angle) and relaxation delays of 4s and 2s for  $^{11}\text{B}$  and  $^{27}\text{Al}$ , respectively. Signal averaging was performed using 600 to 1000 scans per experiment.

$^{31}\text{P}$  MAS NMR data were acquired using a commercial console (VNMRS, Varian) and 3.2mm MAS NMR probe (Chemagnetics), in conjunction with an 11.7 T widebore superconducting magnet and a resonance frequency of 202.30 MHz. Powdered glasses were contained in 3.2 mm zirconia rotors and sample spinning was computer controlled to 20 kHz. Measurement conditions included  $\pi/6$  pulse widths of 1.2  $\mu\text{s}$ , recycle delays of 60s and acquisition of nominally 1500 scans.

MAS NMR spectra for these three nuclei were processed without any additional apodization, plotted using the normal shielding convention and with shift referencing to aqueous boric acid (19.6 ppm), aqueous aluminum nitrate (0.0 ppm) and 85%  $\text{H}_3\text{PO}_4$  solution (0.0 ppm).  $^{11}\text{B}$  and  $^{27}\text{Al}$  MAS NMR data were fit with DMFit utilizing second-order quadrupolar lineshapes for  $^{11}\text{B}$  trigonal peaks, a combination of Gaussian and Lorentzian lineshapes for  $^{11}\text{B}$  tetrahedral resonances, and the CzSimple model for  $^{27}\text{Al}$ <sup>34</sup>. In the case of  $^{11}\text{B}$  MAS NMR data, the overlapping satellite transition for the  $\text{B}^{\text{IV}}$  resonance was also fit and subtracted from the integration, yielding accurate site intensities for all  $\text{B}^{\text{III}}$  and  $\text{B}^{\text{IV}}$  peaks.  $^{31}\text{P}$  MAS NMR data were fit using DMFit and 100% Gaussian lineshapes.

## 2.6 Vickers hardness and elastic moduli

We determined the Vickers hardness ( $H_V$ ) of all glasses using a Nanovea CB500 hardness tester. On each specimen, 20 indents were generated. The loading duration and dwell time were set to 6 s and 10 s, respectively. The residual imprints were subsequently analyzed with an optical microscope and  $H_V$  was calculated as,

$$H_V = 1.8544 \frac{P}{\left(\frac{d_1 + d_2}{2}\right)^2}, \quad (2)$$

where  $P$  is the contact load of 4.9 N, and  $d_1$  and  $d_2$  are the length of the projected indent diagonals.

Furthermore, the elastic properties of the glasses were measured by ultrasonic echography using an ultrasonic thickness gauge (38DL Plus, Olympus) equipped with 20 MHz delay line transducers for the determination of the longitudinal  $V_l$  and transversal wave velocities  $V_t$ . The longitudinal modulus  $C_{11}$ , shear modulus  $G$ , bulk modulus  $B$ , and Young's modulus  $E$ , as well as the Poisson ratio  $\nu$ , were calculated using the following relations, which are applicable for isotropic materials:

$$C_{11} = \rho V_l^2, \quad (3)$$

$$G = \rho V_t^2, \quad (4)$$

$$B = C_{11} - \frac{4}{3}G, \quad (5)$$

$$\nu = \frac{3B - 2G}{6B + 2G}, \quad (6)$$

$$E = 2G(1 + \nu). \quad (7)$$

### 3. Results and Discussion

#### 3.1 Raman spectroscopy

Figure 1a shows the Raman spectra of both as-prepared and compressed lithium phosphoaluminoborate glasses with different content of  $P_2O_5$ . We divide the spectra into four main band regions, with the expected assignments outlined in the following (see also Table S2 in the Supporting Information).

The lowest frequency band region I, ranging from  $\sim 280$  to  $625 \text{ cm}^{-1}$ , is expected to contain contributions originating from B-O-B, Al-O-Al, and B-O-Al stretching<sup>35</sup>. In addition, vibrations due to bending of  $PO_4$  units may occur in this region ( $I_a$ )<sup>36</sup>. We find that the relative intensity of this band region increases with the content of  $P_2O_5$  for the four as-prepared glasses, consistent with a larger concentration of  $PO_4$  units. Band region II ( $\sim 625$  to  $815 \text{ cm}^{-1}$ ) is characteristic for  $B_2O_3$ -rich glasses<sup>35</sup>, since peaks in this frequency range are typically assigned to borate super-structures ( $II_b$ ) such as chain and ring metaborates<sup>37,38</sup>, di-triborates<sup>39</sup>, and penta-, tetra-, or triborates<sup>37,38,39,40</sup>, as well as boroxol rings<sup>37,41</sup>. B-O-Al stretching and aluminate network vibrations may occur in the band  $II_a$  region<sup>42</sup>. The band  $II_b$  region decreases in intensity with the content of  $P_2O_5$ , since the addition of  $P_2O_5$ , and thus removal of  $B_2O_3$ , decreases the fraction of borate super-structures. Band region III ( $\sim 815$  to  $1200 \text{ cm}^{-1}$ ) is expected to result

from vibrations of  $\text{AlO}_4$  units ( $\text{III}_a$ ) ( $\sim 900 \text{ cm}^{-1}$ )<sup>43,44</sup>, Al-B network ( $\sim 980 \text{ cm}^{-1}$ )<sup>45</sup>, borate superstructures ( $\text{III}_b$ ) ( $\sim 930 \text{ cm}^{-1}$ )<sup>35,38</sup> and  $\text{PO}_2^-$ ,  $\text{P}_2\text{O}_7^{4-}$ ,  $\text{PO}_3^{2-}$  units ( $\text{III}_c$ ) ( $\sim 1039\text{-}1090 \text{ cm}^{-1}$ )<sup>46</sup>. We find that the relative intensity of  $\text{III}_a$  band region decreases with the content of  $\text{P}_2\text{O}_5$  for the four as-prepared glasses, since the addition of  $\text{P}_2\text{O}_5$ , and thus removal of  $\text{Al}_2\text{O}_3$ , decreases the probability of forming  $\text{AlO}_4$  units. In addition, the relative intensity of  $\text{III}_c$  band region increases with the content of  $\text{P}_2\text{O}_5$  for the four as-prepared glasses. The bands in region  $\text{III}_b$  lie under those of  $\text{III}_c$ , making it difficult to determine the impact of glass composition on their relative intensities. However, these are minor intensity bands associated with the borate superstructural units contributing to the more intense bands at  $\text{II}_b$ , so dilution of borate groups with increasing  $\text{P}_2\text{O}_5$  is likely to decrease the intensity of bands  $\text{III}_b$  in the same manner as for  $\text{II}_b$ . Finally, a high-frequency region, band region IV ( $\sim 1200$  to  $1600 \text{ cm}^{-1}$ ), is expected to be dominated by contributions from vibrations of superstructural units such as pyroborate units, chain and ring metaborate units<sup>47</sup>. This peak decreases in intensity with the content of  $\text{P}_2\text{O}_5$ , since the addition of  $\text{P}_2\text{O}_5$ , and thus removal of  $\text{B}_2\text{O}_3$ , decreases the fraction of borate superstructures as noted for other regions of these Raman spectra.

Next, we consider the variations in the Raman spectra upon hot compression (Figure 1a). In the glass without  $\text{P}_2\text{O}_5$  (P0 Glass), we find that the area fractions of bands I and II are suppressed with increasing pressure, indicating the breakage of some superstructural borate (and possibly aluminoborate) units. The suppression of bands I and II is accompanied by an increase in the area of bands III and IV upon compression. Considering the P10 glass as an example, Figure 1b shows the pressure dependence of the relative area fractions of the main Raman bands. The area fractions of bands  $\text{I}_b$  and  $\text{II}_b$  decrease significantly with increasing pressure, while that of band  $\text{III}_c$  increases. The other glasses show the same trend upon compression (see Figure S3 in the Supporting Information). The band  $\text{III}_c$  may be ascribed to the formation of  $\text{PO}_2^-$ ,  $\text{P}_2\text{O}_7^{4-}$ ,  $\text{PO}_3^{2-}$  units<sup>46</sup> upon addition of  $\text{P}_2\text{O}_5$ . Hot compression of the P10 glass does not result in the formation of any new bands (Figure 1a), but following the permanent densification, the high-frequency band  $\text{III}_c$  broadens slightly and becomes more intense upon hot compression, especially in high- $\text{P}_2\text{O}_5$  glasses. Such increase in band width can be the result of P-O-P bond angle distortion.

### 3.2 <sup>27</sup>Al MAS NMR spectroscopy

To further understand the effects of  $\text{P}_2\text{O}_5$  addition and compression on the short-range structure of the studied lithium phosphoaluminoborate glasses, we performed <sup>27</sup>Al, <sup>11</sup>B, and <sup>31</sup>P MAS NMR spectroscopy measurements. The spectral deconvolution and determined speciation are shown in Tables S3, S4, S5, and S6 respectively, and Figure S4a in the Supporting Information.

Figure 2 shows the <sup>27</sup>Al MAS NMR spectra for the as-prepared glasses with different content of  $\text{P}_2\text{O}_5$ . The three peaks at about 65, 37, and 9 ppm in the spectrum of the  $\text{P}_2\text{O}_5$ -free glass can be unambiguously assigned to  $\text{Al}^{\text{IV}}$ ,  $\text{Al}^{\text{V}}$ , and  $\text{Al}^{\text{VI}}$ , respectively<sup>20</sup>, as the chemical shifts are similar to those in previous studies

on phosphorous-free aluminoborate and aluminosilicate glasses<sup>23,48,49</sup>. The relative amount of each species is proportional to the corresponding area under its peak, and the fitted values are shown in Table S4 in the Supporting Information. Figure 2 shows that the  $^{27}\text{Al}$  peak position shifts to higher shielding (from 65 to 56 ppm) with increasing  $\text{P}_2\text{O}_5$  content (from 0 to 10 mol%). This is likely due to association of aluminum and phosphorus polyhedra, leading to formation of Al-O-P linkages in the glass network. Such Al-O-P bonding has, however, only a slight effect on the coordination number of aluminum (see below). These results are in agreement with previous studies<sup>20,50</sup>, where for P-containing glasses, the presence of P next-nearest neighbor polyhedra increase the shielding of  $^{27}\text{Al}$  resonances. As demonstrated by the data in Figure 2 and the extracted chemical shifts in Table S4, the impact of  $\text{P}_2\text{O}_5$  on the  $^{27}\text{Al}$  NMR data is seen for all of the resonances, indicating that  $\text{Al}^{\text{IV}}$ ,  $\text{Al}^{\text{V}}$  and  $\text{Al}^{\text{VI}}$  groups are all affected by neighboring phosphate groups, and thus these glasses contain a substantial amount of mixing between aluminate and phosphate polyhedra.

Figure 3 shows the effect of densification on the  $^{27}\text{Al}$  MAS NMR spectra for the four different glasses. Generally, we observe pronounced changes in the aluminum despite the relative modest pressure, in agreement with previous studies on lithium aluminoborate glasses<sup>23</sup>. The areas of the  $\text{Al}^{\text{V}}$  and  $\text{Al}^{\text{VI}}$  peaks increase upon hot compression, corresponding to the conversion of  $\text{Al}^{\text{IV}}$  to  $\text{Al}^{\text{V}}$  and  $\text{Al}^{\text{VI}}$  units, as also found in earlier studies<sup>24,19,25,11</sup>. Consequently, the coordination number of aluminum increases with increasing pressure (Figure 4a). The high- $\text{P}_2\text{O}_5$  glasses have the largest pressure-induced increase in the Al coordination number (from 4.26 to 4.90 for P10 glass) (Figure 4b). In fact, to our knowledge, the extent of the changes in Al speciation for P10 glass are the largest ever reported for an oxide glass under similar pressure/temperature conditions<sup>23,11</sup>. This indicates addition of  $\text{P}_2\text{O}_5$  positively influences the pressure-induced conversion of  $\text{Al}^{\text{IV}}$  to  $\text{Al}^{\text{V}}$  and  $\text{Al}^{\text{VI}}$ , in turn suggesting a link between aluminum and phosphate units as suggested by formation of Al-O-P bonding and the possibility for higher coordinated Al to charge-stabilize phosphate NBOs. Furthermore, we note from Figure 4a that the  $\text{P}_2\text{O}_5$  content has a negligible effect on the Al coordination number in the as-prepared glasses. This could be because it mostly depends on the modifier-to-aluminum ratio (at least in aluminoborosilicate-type glasses), which is not changing in the studied glasses.

The other feature to note in Figure 3 is that the peak positions for the three different Al sites are unaffected by compression. As indicated by the fitting parameters in Table S4, while the intensities of the Al sites vary significantly with compression, the isotropic chemical shifts for each peak are within one ppm from as-made to compression at 2 GPa. This suggests that while  $\text{P}_2\text{O}_5$  content has a strong influence on the chemical shielding of  $^{27}\text{Al}$  resonances, as discussed above for the as-made glasses, the application of hot compression does not appear to change the extent of mixing between aluminum and phosphate polyhedra. That is, the higher shielding exhibited for P-containing glasses is maintained even with structural changes due to compression, consistent with preservation of P NNN even as  $\text{Al}^{\text{IV}}$  is converted to higher coordination number.

### 3.3 $^{11}\text{B}$ MAS NMR spectroscopy

Figure 5 shows the  $^{11}\text{B}$  MAS NMR spectra for the as-prepared glasses with different content of  $\text{P}_2\text{O}_5$ . The glassy networks all consist of both  $\text{B}^{\text{III}}$  (around 5 to 20 ppm) and  $\text{B}^{\text{IV}}$  units (around -2.5 to 5 ppm). The fraction of  $\text{B}^{\text{IV}}$  decreases slightly upon the addition of  $\text{P}_2\text{O}_5$ , indicating that the addition of  $\text{P}_2\text{O}_5$  is beneficial for the conversion of  $\text{B}^{\text{IV}}$  to  $\text{B}^{\text{III}}$ . This could be because the introduced phosphate competes with boron for some of the Li modifiers, leading to fewer Li- $\text{B}^{\text{IV}}$  interactions and thus a lower level of modification of the borate polyhedra. Other changes in the  $^{11}\text{B}$  MAS NMR data are observed with increasing  $\text{P}_2\text{O}_5$ . Arrows in Figure 5 indicate subtle alterations of the  $\text{B}^{\text{III}}$  region of the spectrum, with a slight decrease in intensity at the highest shift side of the signal (around 16-17 ppm), and a corresponding increase in intensity near 10 ppm. Fitting of these data (see Table S3 and Figure S4a in the Supporting Information) provides additional insight into these changes, as deconvolution of the  $\text{B}^{\text{III}}$  lineshape into two distinct  $\text{B}^{\text{III}}$  units can be achieved. As a result, it now is apparent that addition of  $\text{P}_2\text{O}_5$  leads to a direct reduction in the population of the downfield (more positive)  $\text{B}^{\text{III}}$  resonance and an increase in the more shielded (less positive)  $\text{B}^{\text{III}}$  peak intensity. The former is assigned to  $\text{B}^{\text{III}}$  in superstructural units, consistent with some of the Raman spectroscopy features described earlier, and a well-known feature in B-rich glasses<sup>51</sup>. The latter  $\text{B}^{\text{III}}$  signal is attributed to non-ring  $\text{B}^{\text{III}}$ , that is, those  $\text{B}^{\text{III}}$  groups not incorporated into the geometrically constrained environments of borate superstructural units. Thus, increasing  $\text{P}_2\text{O}_5$  content at the expense of  $\text{B}_2\text{O}_3$ , leads to a reduction in the number of ring-type borate groups, which arises due to decreasing  $\text{B}_2\text{O}_3$  content and the inability to maintain the number of such structural groupings. This is analogous to the decreasing intensity of band  $\text{II}_b$  in the Raman spectra of the as-made glasses with increasing  $\text{P}_2\text{O}_5$  content (Figure 1).

The other changes in boron environment with glass composition (no compression) is a slight increase in shielding of the  $\text{B}^{\text{IV}}$  signal (Fig. 5). This is not necessarily easy to see in the stack plot, but after fitting of the  $^{11}\text{B}$  MAS NMR data (Figure S4b in the Supporting Information), the glasses containing  $\text{P}_2\text{O}_5$  required the addition of a second  $\text{B}^{\text{IV}}$  resonance, which was at a more negative shift relative to that in the P0 glass. This peak also increases in relative intensity with increasing  $\text{P}_2\text{O}_5$  content, suggesting a close relation to phosphorus. In fact, the impact of P NNN groups on  $^{11}\text{B}$  shielding is similar to that described above for  $^{27}\text{Al}$  shielding. Interaction of phosphate groups with  $\text{B}^{\text{IV}}$  units leads to a more negative shift, up to the limit of -3.3 ppm found in crystalline  $\text{BPO}_4$ <sup>52</sup>. Studies of P-containing borosilicate glasses indicate that the new peaks formed with  $\text{P}_2\text{O}_5$  addition are consistent with B-O-P linkages involving  $\text{B}^{\text{IV}}$  groups<sup>53</sup>. Thus, the  $\text{B}^{\text{IV}}$  groups in these glasses, while diminishing overall in intensity due to less available modifier, are also being redistributed into network structure having pronounced connectivity between  $\text{B}^{\text{IV}}$  and phosphate polyhedra.

These local boron environments are, like those of aluminum, very sensitive to densification, with boron increasing its average coordination numbers upon compression (see Figure 6)<sup>24,19</sup>. This has been reported to be related to the presence of non-bridging oxygen (NBO), that is,  $\text{B}^{\text{III}} + \text{NBO} \rightarrow \text{B}^{\text{IV}}$ <sup>54</sup>. Indeed,

the  $^{11}\text{B}$  MAS NMR spectra show that the average coordination number of boron increases upon hot compression (Figure 7a). Unlike aluminum, the addition of  $\text{P}_2\text{O}_5$  has a negligible effect on the pressure-induced change in the B coordination number (see Figure 7b), with each glass composition showing similar pressure-induced changes in  $\text{B}^{\text{III}}$  and  $\text{B}^{\text{IV}}$  populations. In addition, there is a small, but noticeable change in the  $\text{B}^{\text{III}}$  peak, near the position previously identified as belonging to ring-type  $\text{B}^{\text{III}}$  units. As seen before in studies of similarly compressed borate and borosilicate glasses<sup>25,55</sup>, the ring  $\text{B}^{\text{III}}$  unit is more strongly impacted by compression, with glass densification accompanied by a decrease in the amount of superstructural units. This is corroborated by the decrease in Raman band  $\text{II}_b$  intensity (Figure 1) as these glasses are compressed at 1 and 2 GPa. The intensity decrease in these bands, as well as the change in ring-type  $\text{B}^{\text{III}}$  peak intensity in these  $^{11}\text{B}$  MAS NMR data, occur similarly for all glasses, regardless of the amount of  $\text{P}_2\text{O}_5$ .

### 3.4 $^{31}\text{P}$ MAS NMR spectroscopy

Figure 8 shows the  $^{31}\text{P}$  MAS NMR spectra for the as-prepared glasses with different content of  $\text{P}_2\text{O}_5$ , with the average peak position moving towards more negative shift values with increasing level of  $\text{P}_2\text{O}_5$ . The  $^{31}\text{P}$  chemical shift is highly sensitive to the immediate geometry of the phosphate tetrahedra (i.e., number of bridging and non-bridging oxygen) and also to the connected (neighboring) polyhedra, with a lower chemical shift corresponding to higher shielding from the groups surrounding phosphorus. In the case of these lithium-modified aluminoborate glasses, there are several possible contributors to the trends exhibited in Figure 8. First, the  $Q^n$  speciation of the phosphate groups may be affected by the overall glass composition, where competition for the lithia modifiers between aluminum, boron, and phosphorus changes with  $\text{P}_2\text{O}_5$  levels. As seen above for both aluminum and boron speciation, these cations are greatly impacted by the alkali, forming both  $\text{Al}^{\text{IV}}$  and  $\text{B}^{\text{IV}}$  tetrahedra in response to the presence of modifier. As  $\text{P}_2\text{O}_5$  is added to the P0 glass, aluminum coordination is mostly unaffected, while boron shows a slight reduction in the fraction of  $\text{B}^{\text{IV}}$  groups, indicating that the added  $\text{P}_2\text{O}_5$  does remove  $\text{Li}^+$  modifiers from mainly the borate portion of the network, and as a result, some of the phosphorus polyhedra will have NBO and thus the phosphate groups are not entirely  $Q^3$  units. This is evidenced by the  $^{31}\text{P}$  MAS NMR data in Figure 8, where the peak position for the P2 glass is centered around -10 ppm, well downfield from the shifts normally found for  $Q^3$  phosphate groups (around -35 to -55 ppm)<sup>56</sup>. According to literature studies of lithium phosphate glasses, the main peak for the P2 glass around -10 ppm lies between those of  $Q^1$  and  $Q^2$  polyhedra<sup>57</sup>, so in neglecting the impact of neighboring polyhedra, this might reflect a mixture of  $Q^1$  and  $Q^2$  phosphate groups in the P2 glass. This simple interpretation would require 2 and 1  $\text{Li}^+$  for each group, respectively, so 1.5  $\text{Li}_2\text{O}$  for every mol of  $\text{P}_2\text{O}_5$ . For the P2 glass, this means that 3 moles of  $\text{Li}_2\text{O}$  would be necessary to form a 50:50 mixture of  $Q^1$  and  $Q^2$  phosphate groups, and given the results above for aluminum and boron speciation, this  $\text{Li}_2\text{O}$  would likely be taken from the boron groups, both seen as a



reduction in  $N_4$  (Fig. 5) and also the concomitant reduction in  $B_2O_3$  content with added  $P_2O_5$  (Table 1). Considering both of these factors, the observation of partially depolymerized phosphate groups is expected. The exact nature of the phosphate groups in the as-made P2 glass is more complicated than this simple “binary” model, as indicated by the deconvolution of the  $^{31}P$  MAS NMR data in the supplemental section (see Figure S4c in the Supporting Information). In this case, at least three resonances are required for fitting, with two of these corresponding directly to  $Q^1$  and  $Q^2$  groups like those in lithium phosphate glasses (e.g., peaks at -6 and -22 ppm, respectively). A third resonance around -13 ppm is necessary, and indicates additional complexity in the phosphate speciation.

Another key contributor to  $^{31}P$  chemical shifts in Al- (and B-) containing glasses is the impact of these other cations when bonded to the phosphate groups. There are five primary possibilities for attaching groups to phosphorus, which all are determined by the chemical shift (see Figure S4 and Table S5 in the Supporting Information). First, we note that the  $^{31}P$  peak of the P10 glass is broadened relative to those with smaller phosphorus content, which could be a result of an increasing amount of phosphorus species present as next nearest neighbors (NNNs). We here denote these as  $Q^n$  units, where  $n$  is the number of bridging oxygens. By deconvolution, we can assign a peak at -6 ppm to  $Q^1$  groups<sup>57</sup> without any Al (or B) NNNs and another peak at -22 ppm to  $Q^2$  groups<sup>57</sup> without any Al (or B) NNNs, showing that there are a substantial amount of P-O-P bonding in the studied glasses. Based on the above analysis, we find that the content of  $B^{IV}$  is relatively low, leading to the fewer B-O-P bonds. This is because B/P association does not typically involve  $B^{III}$ <sup>58</sup>. Since the amount of P with B NNN is low (although the  $^{11}B$  MAS NMR data suggest that it is non-zero), we assume that the various  $Q^n$  groups do not have B NNNs. Instead, we consider the impact of Al as the NNNs, as supported from the steady increase in  $^{27}Al$  NMR shielding above. Although the content of  $B_2O_3$  is higher than that of  $Al_2O_3$  in the glasses, it seems that P/Al association is stronger than P/B, at least for these studied glasses. Therefore, we assign the more intense peak around -13 ppm to  $Q^{1-1}$  groups, which must be a  $Q^1$  phosphate group with one Al NNN. Since replacing the P-O-P with P-O-Al leads to an increased shielding of around 7 ppm<sup>59,60</sup> (the decrease in chemical shift from -6 to -13 ppm), the most plausible assignment is for a  $Q^1$  with one Al NNNs. A very weak peak at 8.5 ppm assigned to the  $Q^0$  groups (i.e., no connectivity with Al or B) is close to that in lithium orthophosphate (10 ppm). Finally, we assign the peak around -29.6 ppm to  $Q^{2-1}$  groups, which is a  $Q^2$  phosphate group with one Al NNN (around 7 ppm increase in shielding). From the deconvolution, we find that the area of the  $Q^1$  units decreases while that of the  $Q^2$  units increases upon the addition of  $P_2O_5$  (Table S5 in the Supporting Information). This indicates that  $Q^1$  units convert to higher  $Q^n$  units, and as a result, the  $^{31}P$  average peak position shifts to higher shielding (from -9.5 to -15.5 ppm) with increasing  $P_2O_5$  content from 2 to 10 mol%.

Figures 9a-c show the effect of densification on the  $^{31}P$  MAS NMR spectra for the three P-containing glasses. Upon hot compression, the  $^{31}P$  peak position slightly increases, which we ascribe to a decrease in the amount of  $P^3$  units and simultaneous increase in  $P^1$  units. In turn, this facilitates the change in Al

coordination, as higher-coordinated Al can serve as a charge compensator for some of the negative charges on these polyhedra. Figure 9d shows that the average  $Q^n$  (P) increases with the addition of  $P_2O_5$ . The increase in the content of  $P_2O_5$  promote B-P association via formation of B-O-P bonds ( $P^2$  and  $P^3$  units), and thus increase the average  $Q^n$  (P). Surprisingly, we note that glasses with higher  $P_2O_5$  content show larger decrease (from -0.041 to -0.087) in the average  $Q^n$  (P) upon compression (Figure 10). Due to the decrease in the average  $Q^n$  (P), there is formation of more NBOs in studied glasses upon pressure. The high-P content can promote the B-P association for the formation of B-O-P units, and thus leading to more pressure-induced depolymerization of B-O-P units ( $P^2$  and  $P^3$  units) for the conversion of  $B^{III}$  to  $B^{IV}$  ( $B^{III} + NBO \rightarrow B^{IV}$ <sup>54</sup>).

### 3.5 Volume densification and self-adaptivity

Figure 11a shows the compositional and pressure dependence of density ( $\rho$ ) before and after hot compression at 1 GPa and 2 GPa. The addition of  $P_2O_5$  has only a slight effect on the density, while the density of each studied glass increases dramatically upon hot compression, which is in agreement with previous work<sup>23,11,17</sup>. Furthermore, since there are also changes in the size of the atoms upon addition of  $P_2O_5$ , we calculate the atomic packing density ( $C_g$ ) to further understand differences in free volume. Figure 11b shows the compositional and pressure dependence of atomic packing density ( $C_g$ ). We can find that  $C_g$  decreases with the content of  $P_2O_5$  for all studied glasses, showing that the network becomes gradually more open with  $P_2O_5$  addition. In order to better understand the difference in the extent of pressure-induced densification for all lithium phosphoaluminoborate glasses, we calculate the irreversible plastic compressibility, i.e., the extent of volume densification following decompression<sup>20</sup>. As shown in Figure 11c, the plastic compressibility decreases with increasing  $P_2O_5$  content. To further understand the relation between volume densification and the short-range order structural changes, we calculated the correlation between plastic compressibility and atomic self-adaptivity (inset Figure 11d). Self-adaptivity is defined the  $(\langle \Delta n \rangle \Delta \rho) / (\rho_0 P)$ , where  $\langle \Delta n \rangle$  is the change in coordination number as determined by NMR,  $\Delta \rho$  is the change in density,  $\rho_0$  is the initial density, and  $P$  is the applied pressure. As such, the ability to self-adapt results from the balance between the energy cost associated with each densification mechanism (inversely correlated to the extent of pressure-induced change in coordination number  $\langle \Delta n \rangle / P$ ), and its efficiency in increasing the packing density (proportional to the accompanying change in density  $\Delta \rho / \rho_0$ ). We find a positive correlation between atomic self-adaptivity and the pressure-induced volume densification. Previous studies<sup>31,24</sup> have shown that  $B^{IV}$  units decrease the extent of densification in borosilicate glasses, whereas  $B^{III}$  units enhance the densification of the glasses due to a more open network and planar structure.

Despite the positive correlation in Figure 11d, the change in the coordination number of boron and aluminum does not constitute the full volume densification. Additional contributions include decrease in the inter-tetrahedral bond angles and the average ring size, and increase in the distribution of network-

former oxygen-bond lengths<sup>61</sup>. To quantify the contribution of the boron and aluminum coordination number changes to the overall pressure-induced volume densification ( $\Delta V_{m(Al+B)}/\Delta V_m$ ), we follow the approach of Wu *et al*<sup>62</sup>. This involves calculating the pressure-induced molar volume change only due to boron and aluminum coordination changes ( $\Delta V_{m(Al+B)}$ ) and the measured pressure-induced molar volume change ( $\Delta V_m$ ).  $\Delta V_{m(Al+B)}$  is calculated as,

$$V_{m(Al+B)} = [X_{Al_2O_3} \sum x_i V_{([i]Al)}] + [X_{B_2O_3} \sum x_i V_{([i]B)}]$$

(8)

where  $X_{Al_2O_3}$  and  $X_{B_2O_3}$  are molar fractions of  $Al_2O_3$  and  $B_2O_3$  in the glass,  $x_i$  is the fraction of Al or B in each coordination state, which is obtained from NMR data (Tables S3 and S4 in the Supporting Information),  $V_{([i]Al)}$  and  $V_{([i]B)}$  are partial molar volumes of  $Al_2O_3$  and  $B_2O_3$  in each coordination state  $i$ . The simplest assumption is that the partial molar volume of each oxide component in a glass is the same as the molar volume of its pure oxide phase. Hence, the molar volume of  $B_2O_3$  with three coordinated boron  $V_{m([3]B)}$  can be approximated as that for pure  $B_2O_3$  glass (38.4 cm<sup>3</sup>/mol) and the molar volume of  $B_2O_3$  with four coordinated boron  $V_{m([4]B)}$  is taken as half of  $V_{m([3]B)}$  (19.2 cm<sup>3</sup>/mol)<sup>62</sup>.  $V_{m([6]Al)}$  can be taken as that for  $\alpha$ -alumina (31.59 cm<sup>3</sup>/mol) and  $V_{m([4]Al)}$  as 37.42 cm<sup>3</sup>/mol.  $V_{m([5]Al)}$  is set to 34.505 cm<sup>3</sup>/mol as the average of its four- and six- coordinated counterparts<sup>62</sup>. As shown in Table 2, we can find that there is a smaller change from 1 to 2 GPa than from ambient to 1 GPa for both the molar volume ( $V_m$ ) and  $V_{m(Al+B)}$  upon hot compression. The contribution of the boron and aluminum coordination number changes to the overall pressure-induced densification can be expressed by the ratio  $\Delta V_{m(Al+B)}/\Delta V_m$ , with contributions above 50% at 2 GPa (Table 2). This is a large proportion of the pressure-induced volume densification compared to that found for calcium aluminoborosilicate glasses (9-36% at 2 GPa)<sup>62</sup>. This is likely because the present glasses have more pronounced coordination number changes of Al and B upon compression, which in turn is due to the high concentration of  $B_2O_3$  and  $Al_2O_3$  and lithium as modifier. That is, reassociation of charge-balancing modifier cations from  $Al^{IV}$  to  $B^{IV}$  sites is required upon compression, which is promoted by the mobility of small lithium cations<sup>23</sup>. As shown in Table 2, we also find that the  $V_{m(Al+B)}$  contribution to the overall change in measured  $V_m$  becomes smaller with increasing content of  $P_2O_5$ , matching the compositional trend in self-adaptivity (Figure S5 in the Supporting Information). This is expected since phosphorous does not contribute to the coordination number changes, but only to changes in  $Q$ -speciation with limited differences in partial molar volume<sup>20</sup>.

### 3.6 Glass properties: $T_g$ , elastic moduli, and hardness

Figure 12 shows the compositional evolution of the glass transition temperature ( $T_g$ ). We can find that the addition of  $P_2O_5$  leads to a slight increase in the  $T_g$  of the lithium phosphoaluminoborate glasses. This indicates that the addition of  $P_2O_5$  results in a more rigid glass network, i.e., more atomic constraints per

atom, which has been shown in earlier work to be positively correlated with higher glass transition temperature<sup>20</sup>.

Next, we measured the elastic moduli and Poisson's ratio ( $\nu$ ) for the as-prepared and hot compressed glasses (Figure 13a and Figure S6 in the Supporting Information). As seen for glass transition temperature, the addition of  $P_2O_5$  has only a relatively small effect on the elastic moduli for all studied glasses. There is a slight decrease in elastic moduli with the  $P_2O_5$  content. Elastic moduli generally increase with the bond strength and the number of bonds per volume<sup>63</sup>. Recent topological models have found  $E$  to be positively correlated with the volumetric constraint density<sup>64,65</sup>. That is, the number of constraints per volume decreases significantly with addition of  $P_2O_5$ , which is mainly as a result of the decrease of  $C_g$  with  $P_2O_5$  (Fig. 11b). This is because the number of constraints per atom only increases slightly when considering the relatively small variation in  $T_g$  (Fig. 12).

The role of packing density on elastic moduli is also seen from the pressure-induced increase in all elastic moduli, as consistent with previous findings<sup>17,11</sup>. Indeed, packing density scales positively with  $E$  across pressures and compositions (Fig. 13b). We note that the elastic moduli also exhibit record high changes (e.g., 59% increase in  $E$  for P2 glass upon compression at 2 GPa) as a result of compression (Table S1), which is in agreement with the high extent of permanent volume densification exhibited by the studied glass composition in comparison to other oxide glasses<sup>11,17</sup>. Although the elastic moduli are thus easily changed by compression, Vickers hardness is even more sensitive to the pressure treatment (see below), resulting in a decrease in the elastoplastic ratio  $E/H$  with increasing pressure (Figure S6d in the Supporting Information).

Figure 14a shows the compositional and pressure dependence of Vickers hardness ( $H_V$ ), with the addition of  $P_2O_5$  having a negative effect on  $H_V$ . Furthermore, we find that  $H_V$  increases upon hot compression, which is in agreement with the previous works<sup>23,11,17</sup>. The packing density increases and hence the number of atomic bond constraints per unit volume also increases upon hot compression, resulting in the increase of the Vickers hardness (Figure 14b). Furthermore, the extent of the increase in Vickers hardness upon 2 GPa compression is more pronounced in glasses with higher plastic compressibility (Figure 11c) and lower network former coordination numbers changes (Figure S7 in the Supporting Information). However, the  $H_V$  vs.  $C_g$  trend is not perfect (Fig. 14b), suggesting that the pressure-induced increase in packing density is not the only reason for the increase in hardness. Indeed, the coordination numbers of the network-forming boron and aluminum cations increase upon compression (Figure S7 in the Supporting Information), resulting in more bond constraints per atom, and thus also contributes to the increase of Vickers hardness.

#### 4. Conclusions

In this study, we have investigated the influence of composition and hot compression on the structure and mechanical properties of lithium phosphoaluminoborate glasses. The addition of  $P_2O_5$  partially disturbs the aluminoborate network through the formation of mainly P-O-Al and some P-O-B units, thus decrease the atomic packing density. The  $P_2O_5$  addition also results in a minor decrease in the coordination number of boron, but no change in that of aluminum. The introduced phosphate thus competes with boron for some of the Li modifiers, leading to fewer Li-B<sup>IV</sup> interactions. The average  $Q^n$  (P) increases with the addition of  $P_2O_5$ , as more  $P_2O_5$  promotes formation of B-O-P bonds ( $P^2$  and  $P^3$  units), and thus increases the average  $Q^n$  (P). The cation-oxygen coordination numbers of both boron and aluminum increase upon hot compression, while the average  $Q^n$  (P) decreases. The high- $P_2O_5$  glasses have the largest pressure-induced increase in the Al coordination number (from 4.26 to 4.90 for P10 glass) and largest decrease in the average  $Q^n$  (P), resulting in the formation of more NBOs in the compressed glasses, indicating that the higher coordinated Al units are needed to charge-stabilize phosphate NBOs. The B and Al coordination number changes are found to contribute significantly (around 50% at 2 GPa) to the overall volume densification, which is significantly higher than that found in silicate glasses. The increases in bond constraint density (due to volume densification) and network rigidity (due to higher average coordination number) are responsible for the pressure-induced increase in hardness and elastic moduli.

### Acknowledgements

This work was supported by the China Scholarship Council (CSC No. 201806370210).

## References

1. Mostofa MG, Park CI, Park SS. AFM Probe Based Nano Mechanical Scribing of Soda-Lime Glass. *J. Manuf. Process.* 2013; 15(4):625-634.
2. Brambilla G, Payne DN. The Ultimate Strength of Glass Silica Nanowires. *Nano Lett.* 2009; 9(2):831-835.
3. Frankberg EJ, Kalikka J, García Ferré F, Joly-Pottuz L, Salminen T, Hintikka J, et al. Highly Ductile Amorphous Oxide at Room Temperature and High Strain Rate. *Science.* 2019; 366(6467):864-869.
4. Wondraczek L, Mauro JC, Eckert J, Kühn U, Horbach J, Deubener J, et al. Towards Ultrastrong Glasses. *Adv. Mater.* 2011; 23(39):4578-4586.
5. Ritter JE, Sherburne CL. Dynamic and Static Fatigue of Silicate Glasses. *J. Am. Ceram. Soc.* 1971; 54(12):601-605.
6. Kurkjian CR, Gupta PK, Brow RK. The Strength of Silicate Glasses: What Do We Know, What Do We Need to Know? *Int. J. Appl. Glas. Sci.* 2010; 1(1):27-37.
7. Mercier M, Di Muro A, Giordano D, Métrich N, Lesne P, Pichavant M, et al. Influence of Glass Polymerisation and Oxidation on Micro-Raman Water Analysis in Alumino-Silicate Glasses. *Geochim. Cosmochim. Acta* 2009; 73(1):197-217.
8. Sglavo VM, Prezzi A, Zandonella T. Engineered Stress-Profile Silicate Glass: High Strength Material Insensitive to Surface Defects and Fatigue. *Adv. Eng. Mater.* 2004; 6(5):344-349.
9. Gupta PK, Mauro JC. Composition Dependence of Glass Transition Temperature and Fragility. I. A Topological Model Incorporating Temperature-Dependent Constraints. *J. Chem. Phys.* 2009; 130(9):094503.
10. Mauro JC, Tandia A, Vargheese KD, Mauro YZ, Smedskjaer MM. Accelerating the Design of Functional Glasses through Modeling. *Chem. Mater.* 2016; 28(12): 4267-4277.
11. Kapoor S, Wondraczek L, Smedskjaer MM. Pressure-Induced Densification of Oxide Glasses at the Glass Transition. *Front. Mater.* 2017; 4:1-20.
12. Januchta K, Stepniewska M, Jensen LR, Zhang Y, Somers MAJ, Bauchy M, et al. Breaking the Limit of Micro-Ductility in Oxide Glasses. *Adv. Sci.* 2019; 6(18):1901281.
13. Peter KW. Densification and Flow Phenomena of Glass in Indentation Experiments. *J. Non. Cryst.*

- Solids. 1970; 5(2):103-115.
14. Rouxel T, Ji H, Guin JP, Augereau F, Rufflé B. Indentation Deformation Mechanism in Glass: Densification versus Shear Flow. *J. Appl. Phys.* 2010; 107(9):094903.
  15. Yoshida S, Sanglebœuf JC, Rouxel T. Quantitative Evaluation of Indentation-Induced Densification in Glass. *J. Mater. Res.* 2005; 20(12):3404-3412.
  16. Yoshida S, Sawasato H, Sugawara T, Miura Y, Matsuoka J. Effects of Indenter Geometry on Indentation-Induced Densification of Soda-Lime Glass. *J. Mater. Res.* 2010; 25(11):2203-2211.
  17. Svenson MN, Guerette M, Huang L, Lönnroth N, Mauro JC, Rzoska SJ, et al. Universal Behavior of Changes in Elastic Moduli of Hot Compressed Oxide Glasses. *Chem. Phys. Lett.* 2016; 651:88-91.
  18. Deschamps T, Margueritat J, Martinet C, Mermet A, Champagnon B. Elastic Moduli of Permanently Densified Silica Glasses. *Sci. Rep.* 2015; 4(1):7193.
  19. Bechgaard TK, Goel A, Youngman RE, Mauro JC, Rzoska SJ, Bockowski M, et al. Structure and Mechanical Properties of Compressed Sodium Aluminosilicate Glasses: Role of Non-Bridging Oxygens. *J. Non. Cryst. Solids.* 2016; 441:49-57.
  20. Kapoor S, Guo X, Youngman RE, Hogue CL, Mauro JC, Rzoska SJ, et al. Network Glasses Under Pressure: Permanent Densification in Modifier-Free  $\text{Al}_2\text{O}_3$ - $\text{B}_2\text{O}_3$ - $\text{P}_2\text{O}_5$ - $\text{SiO}_2$  Systems. *Phys. Rev. Appl.* 2017; 7(5):054011.
  21. Smedskjaer MM, Bauchy M, Mauro JC, Rzoska SJ, Bockowski M. Unique Effects of Thermal and Pressure Histories on Glass Hardness: Structural and Topological Origin. *J. Chem. Phys.* 2015; 143(16):164505.
  22. Lee SK, Mun KY, Kim Y, Lhee J, Okuchi T, Lin J. Degree of Permanent Densification in Oxide Glasses upon Extreme Compression up to 24 GPa at Room Temperature. *J. Phys. Chem. Lett.* 2020; 11(8):2917-2924.
  23. Januchta K, Youngman RE, Goel A, Bauchy M, Logunov SL, Rzoska SJ, et al. Discovery of Ultra-Crack-Resistant Oxide Glasses with Adaptive Networks. *Chem. Mater.* 2017; 29(14):5865-5876.
  24. Svenson MN, Bechgaard TK, Fuglsang SD, Pedersen RH, Tjell AØ, Østergaard MB, et al. Composition-Structure-Property Relations of Compressed Borosilicate Glasses. *Phys. Rev. Appl.* 2014; 2(2):024006.
  25. Østergaard MB, Youngman RE, Svenson MN, Rzoska SJ, Bockowski M, Jensen LR, et al. Temperature-Dependent Densification of Sodium Borosilicate Glass. *RSC Adv.* 2015; 5(96):78845-

78851.

26. Januchta K, Bauchy M, Youngman RE, Rzoska SJ, Bockowski M, Smedskjaer MM. Modifier Field Strength Effects on Densification Behavior and Mechanical Properties of Alkali Aluminoborate Glasses. *Phys. Rev. Mater.* 2017; 1(6):063603.
27. Januchta K, Youngman RE, Goel A, Bauchy M, Rzoska SJ, Bockowski M, et al. Structural Origin of High Crack Resistance in Sodium Aluminoborate Glasses. *J. Non. Cryst. Solids.* 2017; 460:54-65.
28. Frederiksen KF, Januchta K, Mascaraque N, Youngman RE, Bauchy M, Rzoska SJ, et al. Structural Compromise between High Hardness and Crack Resistance in Aluminoborate Glasses. *J. Phys. Chem. B.* 2018; 122(23):6287-6295.
29. Liu P, Januchta K, Jensen LR, Bauchy M, Smedskjaer MM. Competitive Effects of Free Volume, Rigidity, and Self-adaptivity on Indentation Response of Silicoaluminoborate Glasses. *J. Am. Ceram. Soc.* 2020; 103(2):944-954.
30. Dickinson JE, de Jong BHWS, Schramm CM. Hydrogen-Containing Glass and Gas-Ceramic Microfoams: Raman, XPS, and MAS-NMR Results on the Structure of Precursor  $\text{SiO}_2\text{-B}_2\text{O}_3\text{-P}_2\text{O}_5$  Glasses. *J. Non. Cryst. Solids.* 1988; 102(1-3):196-204.
31. KATO Y, YAMAZAKI H, KUBO Y, YOSHIDA S, MATSUOKA J, AKAI T. Effect of  $\text{B}_2\text{O}_3$  Content on Crack Initiation under Vickers Indentation Test. *J. Ceram. Soc. Japan.* 2010; 118(1381):792-798.
32. Smedskjaer MM, Rzoska SJ, Bockowski M, Mauro JC. Mixed Alkaline Earth Effect in the Compressibility of Aluminosilicate Glasses. *J. Chem. Phys.* 2014; 140(5):054511.
33. Shannon RD. Revised Effective Ionic Radii and Systematic Studies of Interatomic Distances in Halides and Chalcogenides. *Acta Crystallogr. Sect. A.* 1976; 32(5):751-767.
34. Massiot D, Fayon F, Capron M, King I, Le Calvé S, Alonso B, et al. Modelling One- and Two-Dimensional Solid-State NMR Spectra. *Magn. Reson. Chem.* 2002; 40(1):70-76.
35. Li H, Su Y, Li L, Strachan DM. Raman Spectroscopic Study of Gadolinium(III) in Sodium-Aluminoborosilicate Glasses. *J. Non. Cryst. Solids.* 2001; 292(1-3):167-176.
36. Lai YM, Liang XF, Yang SY, Wang JX, Zhang BT. Raman Spectra Study of Iron Phosphate Glasses with Sodium Sulfate. *J. Mol. Struct.* 2012; 1013:134-137.
37. Konijnendijk WL, Stevels JM. The Structure of Borosilicate Glasses Studied by Raman Scattering. *J. Non. Cryst. Solids.* 1976; 20(2):193-224.



38. Kamitsos EI, Chryssikos GD. Borate Glass Structure by Raman and Infrared Spectroscopies. *J. Mol. Struct.* 1991; 247(C):1-16.
39. Meera BN, Ramakrishna J. Raman Spectral Studies of Borate Glasses. *J. Non. Cryst. Solids.* 1993; 159(1-2):1-21.
40. Vignarooban K, Boolchand P, Micoulaut M, Malki M, Bresser WJ. Rigidity Transitions in Glasses Driven by Changes in Network Dimensionality and Structural Groupings. *Europhysics. Lett.* 2014; 108(5):56001.
41. Krogh-Moe J. The Structure of Vitreous and Liquid Boron Oxide. *J. Non. Cryst. Solids.* 1969; 1(4):269-284.
42. Hudgens JJ, Brow RK, Tallant DR, Martin SW. Raman Spectroscopy Study of the Structure of Lithium and Sodium Ultraphosphate Glasses. *J. Non. Cryst. Solids.* 1998; 223(1-2):21-31.
43. McMillan P, Piriou B. Raman Spectroscopy of Calcium Aluminate Glasses and Crystals. *J. Non. Cryst. Solids.* 1983; 55(2):221-242.
44. Licheron M, Montouillout V, Millot F, Neuville DR. Raman and  $^{27}\text{Al}$  NMR Structure Investigations of Aluminate Glasses:  $(1-x)\text{Al}_2\text{O}_3\text{-}x\text{MO}$ , with  $\text{M}=\text{Ca, Sr, Ba}$  and  $0.5 < x < 0.75$ ). *J. Non. Cryst. Solids.* 2011; 357(15):2796-2801.
45. Ollier N, Charpentier T, Boizot B, Wallez G, Ghaleb D. A Raman and MAS NMR Study of Mixed Alkali Na-K and Na-Li Aluminoborosilicate Glasses. *J. Non. Cryst. Solids.* 2004; 341(1-3):26-34.
46. Le Saoût G, Simon P, Fayon F, Blin A, Vaills Y. Raman and Infrared Study of  $(\text{PbO})_x(\text{P}_2\text{O}_5)_{(1-x)}$  Glasses. *J. Raman Spectrosc.* 2002; 33(9):740-746.
47. Yano T, Kunimine N, Shibata S, Yamane M. Structural Investigation of Sodium Borate Glasses and Melts by Raman Spectroscopy. *J. Non. Cryst. Solids.* 2003; 321(3):137-146.
48. Weber R, Sen S, Youngman RE, Hart RT, Benmore CJ. Structure of High Alumina Content  $\text{Al}_2\text{O}_3\text{-SiO}_2$  Composition Glasses. *J. Phys. Chem. B.* 2008; 112(51):16726-16733.
49. Du LS, Stebbins JF. Site Connectivities in Sodium Aluminoborate Glasses: Multinuclear and Multiple Quantum NMR Results. *Solid State Nucl. Magn. Reson.* 2005; 27(1-2):37-49.
50. Aitken BG, Youngman RE, Deshpande RR, Eckert H. Structure-Property Relations in Mixed-Network Glasses: Multinuclear Solid State NMR Investigations of the System  $x\text{Al}_2\text{O}_3\text{:}(30-x)\text{P}_2\text{O}_5\text{:}70\text{SiO}_2$ . *J. Phys. Chem. C.* 2009; 113(8):3322-3331.

51. Youngman RE, Zwanziger JW. Network Modification in Potassium Borate Glasses: Structural Studies with NMR and Raman Spectroscopies. *J. Phys. Chem.* 1996; 100(41):16720-16728.
52. Turner GL, Smith KA, Kirkpatrick RJ, Oldfield E. Boron-11 Nuclear Magnetic Resonance Spectroscopic Study of Borate and Borosilicate Minerals and a Borosilicate Glass. *J. Magn. Reson.* 1986; 67(3):544-550.
53. Michaelis VK, Kachhadia P, Kroeker S. Clustering in Borate-Rich Alkali Borophosphate Glasses: A  $^{11}\text{B}$  and  $^{31}\text{P}$  MAS NMR Study. *Phys. Chem. Glas. Eur. J. Glas. Sci. Technol. Part B.* 2013; 54(1):20-26.
54. Bista S, Morin EI, Stebbins JF. Response of Complex Networks to Compression: Ca, La, and Y Aluminoborosilicate Glasses Formed from Liquids at 1 to 3 GPa Pressures. *J. Chem. Phys.* 2016; 144(4):044502.
55. Svenson MN, Youngman RE, Yue Y, Rzoska SJ, Bockowski M, Jensen LR, et al. Volume and Structural Relaxation in Compressed Sodium Borate Glass. *Phys. Chem. Chem. Phys.* 2016; 18(43):29879-29891.
56. Brow RK. Review: The Structure of Simple Phosphate Glasses. *J. Non. Cryst. Solids.* 2000; 263-264:1-28.
57. van Wüllen L, Eckert H, Schwering G. Structure-Property Correlations in Lithium Phosphate Glasses: New Insights from  $^{31}\text{P} \leftrightarrow ^7\text{Li}$  Double-Resonance NMR. *Chem. Mater.* 2000; 12(7):1840-1846.
58. Uesbeck T, Eckert H, Youngman R, Aitken B. The Structure of Borophosphosilicate Pure Network Former Glasses Studied by Multinuclear NMR Spectroscopy. *J. Phys. Chem. C.* 2017; 121(3):1838-1850.
59. Cody GD, Mysen B, Sághi-Szabó G, Tossell JA. Silicate-Phosphate Interactions in Silicate Glasses and Melts: I. A Multinuclear ( $^{27}\text{Al}$ ,  $^{29}\text{Si}$ ,  $^{31}\text{P}$ ) MAS NMR and Ab Initio Chemical Shielding ( $^{31}\text{P}$ ) Study of Phosphorous Speciation in Silicate Glasses. *Geochim. Cosmochim. Acta.* 2001; 65(14):2395-2411.
60. Brow RK, Kirkpatrick RJ, Turner GL. Local Structure of  $\text{XAl}_2\text{O}_3(1-x)\text{NaPO}_3$  Glasses: An NMR and XPS Study. *J. Am. Ceram. Soc.* 1990; 73(8):2293-2300.
61. Wu J, Deubener J, Stebbins JF, Grygarova L, Behrens H, Wondraczek L, et al. Structural Response of a Highly Viscous Aluminoborosilicate Melt to Isotropic and Anisotropic Compressions. *J. Chem. Phys.* 2009; 131(10):104504.

62. Wu J, Gross TM, Huang L, Jaccani SP, Youngman RE, Rzoska SJ, et al. Composition and Pressure Effects on the Structure, Elastic Properties and Hardness of Aluminoborosilicate Glass. *J. Non. Cryst. Solids*. 2020; 530:119797.
63. Rouxel T. Elastic Properties and Short-to Medium-Range Order in Glasses. *J. Am. Ceram. Soc.* 2007; 90(10):3019-3039.
64. Wilkinson CJ, Zheng Q, Huang L, Mauro JC. Topological Constraint Model for the Elasticity of Glass-Forming Systems. *J. Non-Crystalline Solids X*. 2019; 2:100019.
65. Yang K, Yang B, Xu X, Hoover C, Smedskjaer MM, Bauchy M. Prediction of the Young's Modulus of Silicate Glasses by Topological Constraint Theory. *J. Non. Cryst. Solids*. 2019; 514:15-19.

## TABLES

**Table 1.** Analyzed chemical compositions of the lithium phosphoaluminoborate glasses (in mol%). The uncertainty is around  $\pm 1\%$ .

Glass ID	P <sub>2</sub> O <sub>5</sub>	B <sub>2</sub> O <sub>3</sub>	Al <sub>2</sub> O <sub>3</sub>	Li <sub>2</sub> O
<b>P0</b>	0	53.6	20.7	25.7
<b>P2</b>	2.2	51.8	20.9	25.1
<b>P5</b>	4.9	50.9	20.4	23.8
<b>P10</b>	9.7	46.5	21.6	22.2

**Table 2.** Estimation of volume changes based on the boron and aluminum coordination changes between as-prepared and compressed glasses ( $\Delta V_{m(\text{Al+B})}$ ) by Eq. (8) and the measured molar volume changes between as-made and compressed glasses ( $\Delta V_m$ ).

Glass	P0 Glass	P2 Glass	P5 Glass	P10 Glass
$\Delta V_m$ at 1 GPa (cm <sup>3</sup> /mol)	2.40	2.38	2.38	2.38
$\Delta V_m$ at 2 GPa (cm <sup>3</sup> /mol)	3.79	3.73	3.82	3.91
$\Delta V_{m(\text{Al+B})}$ at 1 GPa (cm <sup>3</sup> /mol)	1.05	1.04	1.03	0.88
$\Delta V_{m(\text{Al+B})}$ at 2 GPa (cm <sup>3</sup> /mol)	2.02	1.97	2.01	1.88
$\Delta V_{m(\text{Al+B})}/\Delta V_m$ at 1 GPa	43.8%	43.7%	43.3%	37.0%
$\Delta V_{m(\text{Al+B})}/\Delta V_m$ at 2 GPa	53.3%	52.8%	52.6%	48.1%

## LIST OF TABLE AND FIGURE CAPTIONS

**Table 1.** Analyzed chemical compositions of the lithium phosphoaluminoborate glasses (in mol%). The uncertainty is around  $\pm 1\%$ .

**Table 2.** Estimation of volume changes based on the boron and aluminum coordination changes between as-prepared and compressed glasses ( $\Delta V_{m(\text{Al+B})}$ ) by Eq. (8) and the measured molar volume changes between as-made and compressed glasses ( $\Delta V_m$ ).

**Figure 1.** (a) Micro-Raman spectra of the as-prepared and compressed lithium phosphoaluminoborate glasses with different content of  $\text{P}_2\text{O}_5$  (see sample IDs in Table 1). The spectra are divided into four main different band regions. (b) Pressure dependence of the relative area fractions of the main Raman bands in the P10 glass.

**Figure 2.**  $^{27}\text{Al}$  MAS NMR spectra for the as-prepared lithium phosphoaluminoborate glasses with different content of  $\text{P}_2\text{O}_5$ .

**Figure 3.** Effect of hot compression on the  $^{27}\text{Al}$  MAS NMR spectra for (a) P0 glass, (b) P2 glass, (c) P5 glass, and (d) P10 glass.

**Figure 4.** (a) Composition and pressure dependence of the average coordination number (CN) of aluminum. (b) Composition dependence of the change in aluminum coordination number with pressure ( $\Delta\text{CN}/P$ ). The error in aluminum's CN is around  $\pm 0.02$ .

**Figure 5.**  $^{11}\text{B}$  MAS NMR spectra for the as-prepared lithium phosphoaluminoborate glasses with different content of  $\text{P}_2\text{O}_5$ . Arrows indicate changes in the direction of increasing  $\text{P}_2\text{O}_5$  content.

**Figure 6.** Effect of hot compression on the  $^{11}\text{B}$  MAS NMR spectra for (a) P0 glass, (b) P2 glass, (c) P5 glass, and (d) P10 glass.

**Figure 7.** (a) Composition and pressure dependence of the average coordination number (CN) of boron. (b) Composition dependence of the change in boron coordination number with pressure ( $\Delta\text{CN}/P$ ). The error in boron's CN is around  $\pm 0.01$ .

**Figure 8.**  $^{31}\text{P}$  MAS NMR spectra for the as-prepared lithium phosphoaluminoborate glasses with different content of  $\text{P}_2\text{O}_5$ .

**Figure 9.** Effect of pressure on the  $^{31}\text{P}$  MAS NMR spectra for (a) P2 glass, (b) P5 glass, and (c) P10 glass. (d) Composition and pressure dependence of the average  $Q^n(P)$ .

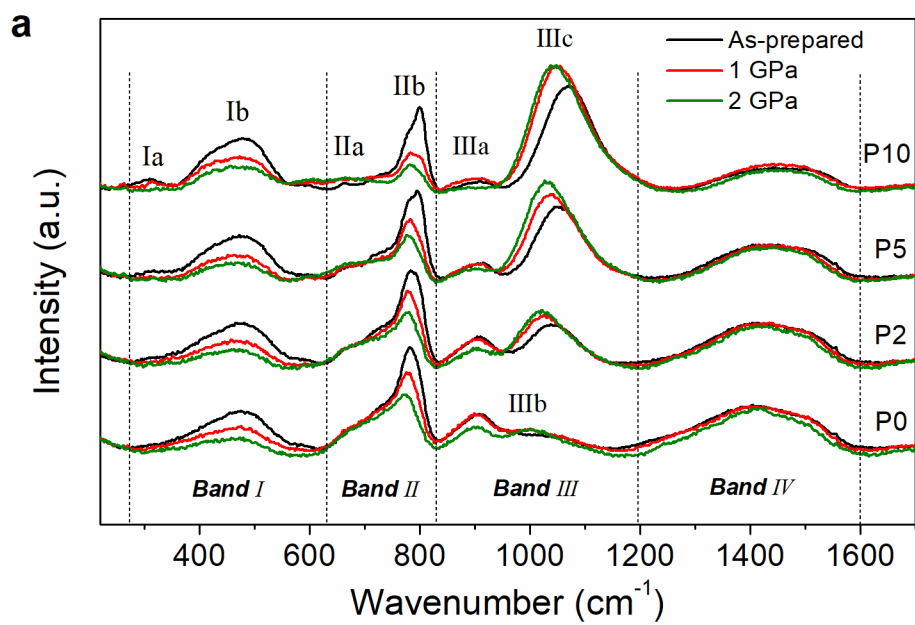
**Figure 10.** Composition dependence of the change in phosphorous speciation with pressure ( $\Delta Q^n/P$ ).

**Figure 11.** Compositional and pressure dependence of (a) density ( $\rho$ ) and (b) atomic packing density ( $C_g$ ). (c) Composition dependence of plastic compressibility. (d) Correlation between plastic compressibility and atomic self-adaptivity.

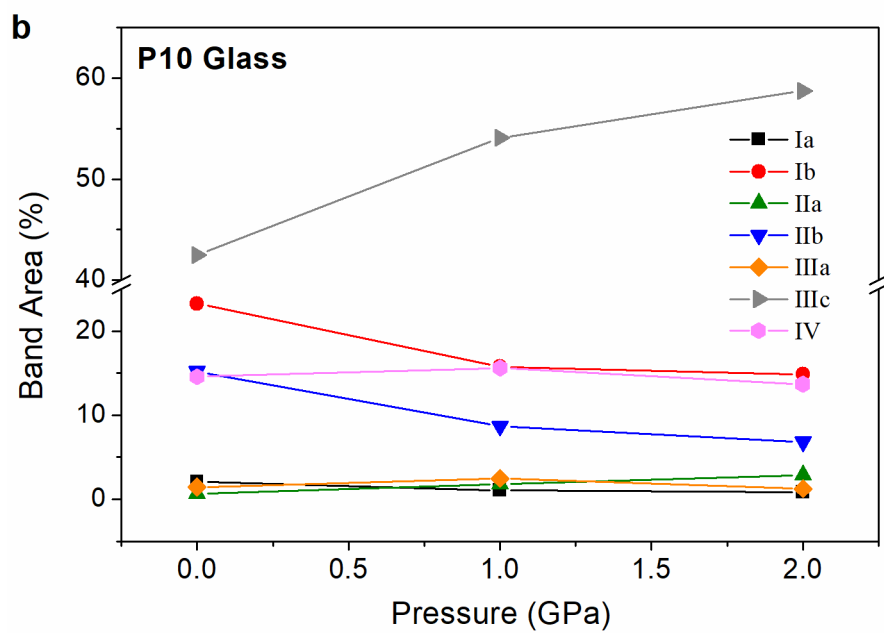
**Figure 12.** Composition dependence of the glass transition temperature ( $T_g$ ) for as-prepared lithium phosphoaluminoborate glasses with different content of  $\text{P}_2\text{O}_5$ . The error in  $T_g$  does not exceed  $2^\circ\text{C}$ .

**Figure 13.** (a) Compositional and pressure dependences of the elastic moduli (Young's ( $E$ )) in the lithium phosphoaluminoborate glasses. (b) The relation between Young's modulus and atomic packing density.

**Figure 14.** (a) Compositional and pressure dependence of Vickers hardness ( $H_V$ ) in the lithium phosphoaluminoborate glasses. (b) The relation between Vickers hardness and atomic packing density.

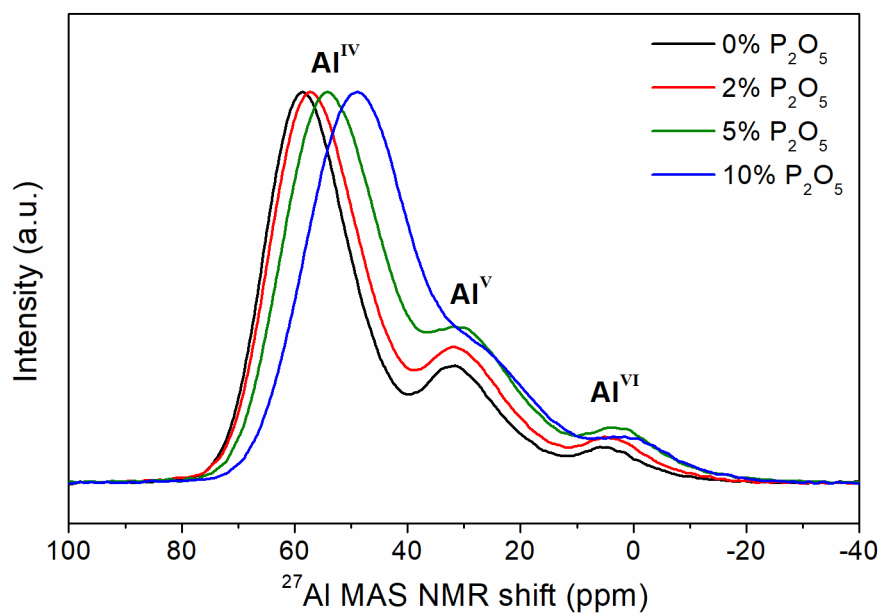


jace\_17559\_f1a.tif

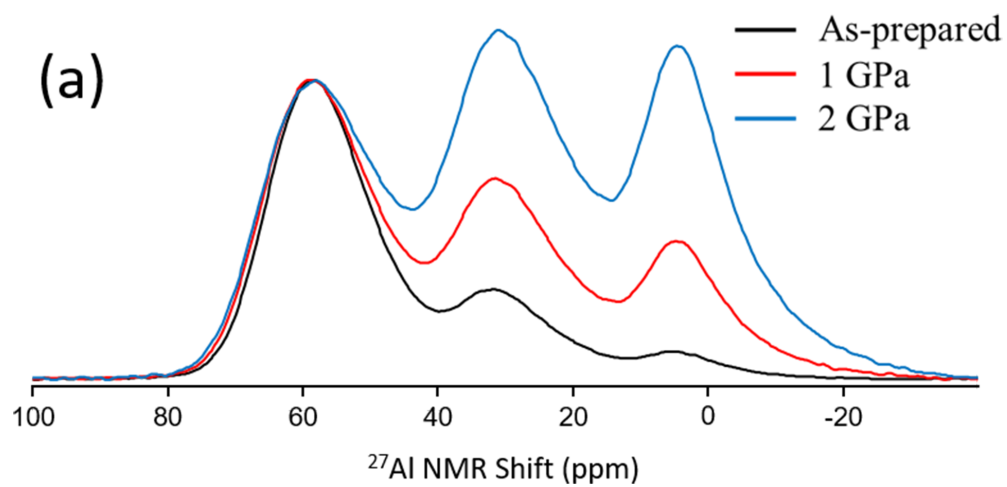


jace\_17559\_f1b.tif

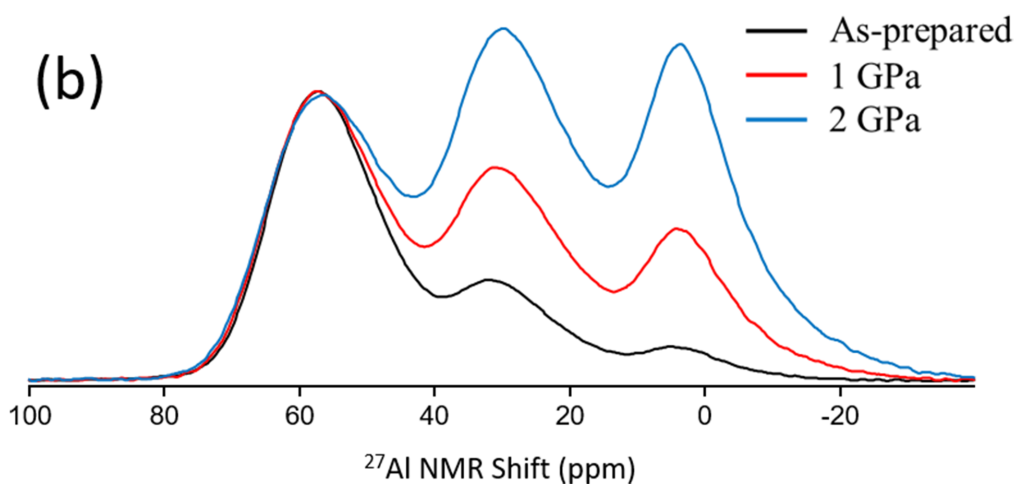




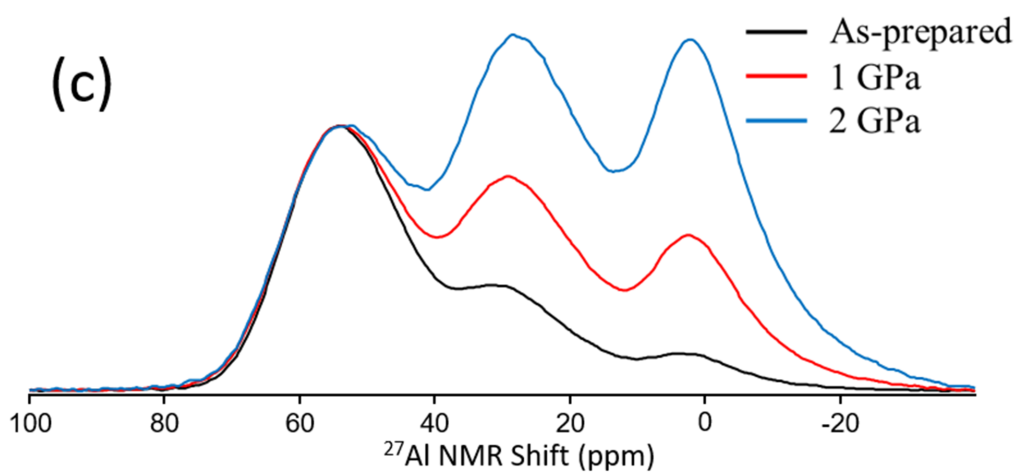
jace\_17559\_f2.tif



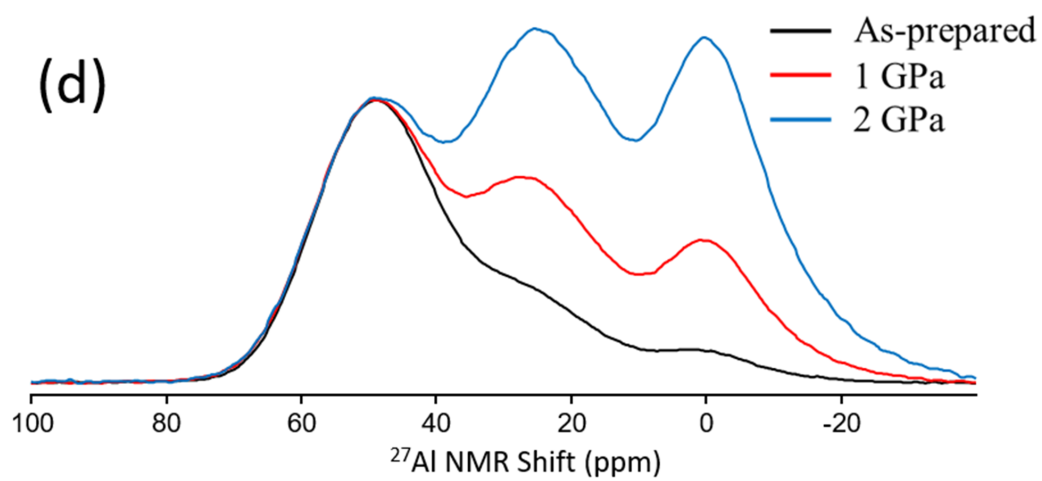
jace\_17559\_f3a.tif



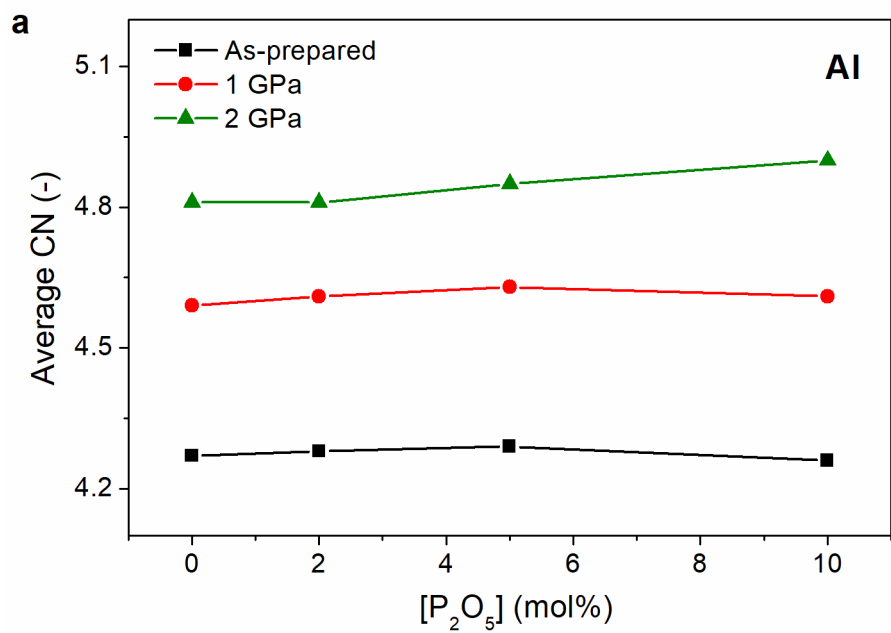
jace\_17559\_f3b.tif



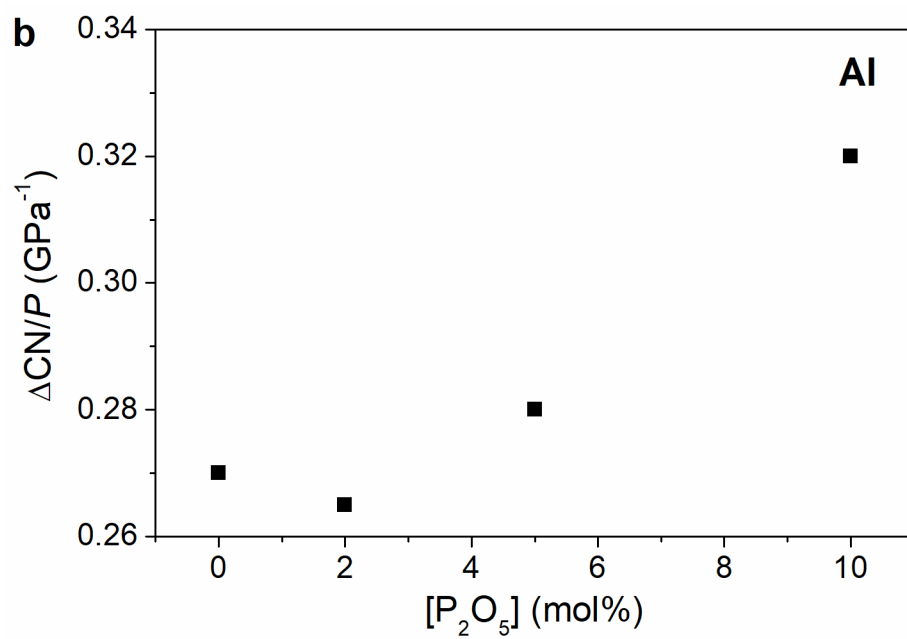
jace\_17559\_f3c.tif



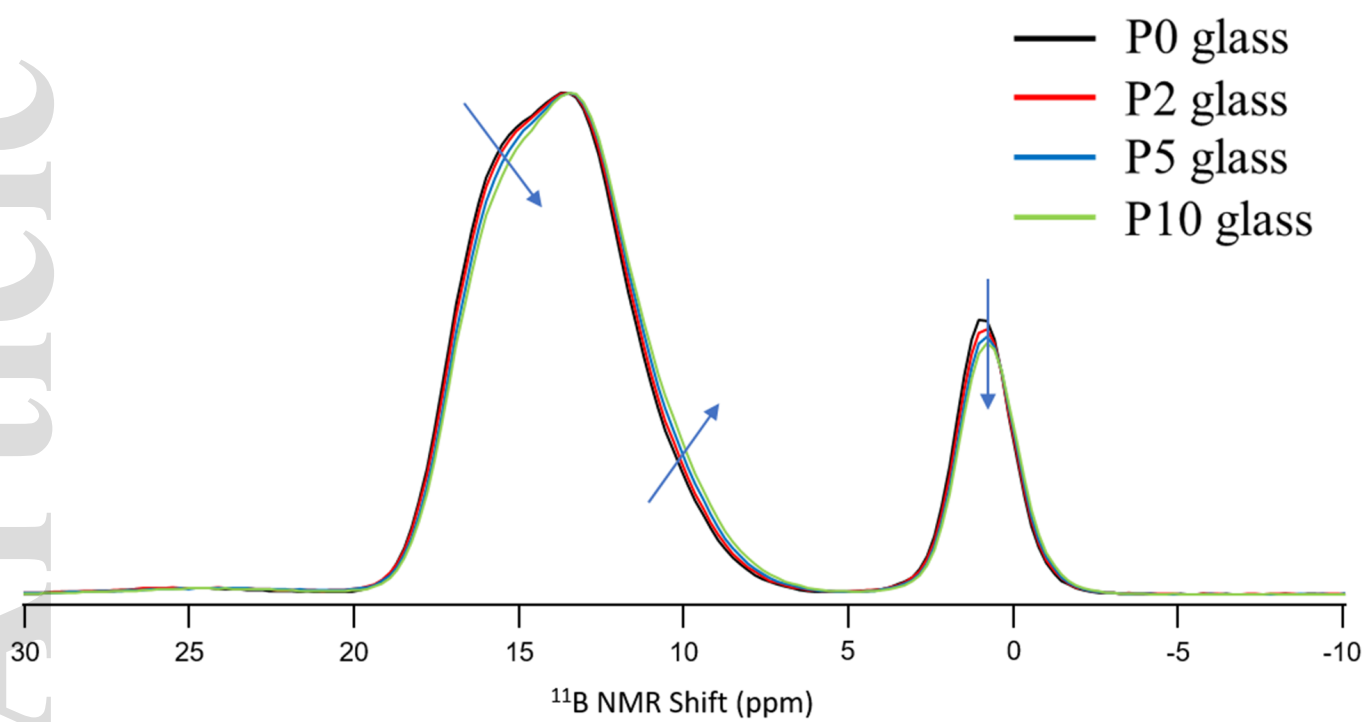
jace\_17559\_f3d.tif



jace\_17559\_f4a.tif

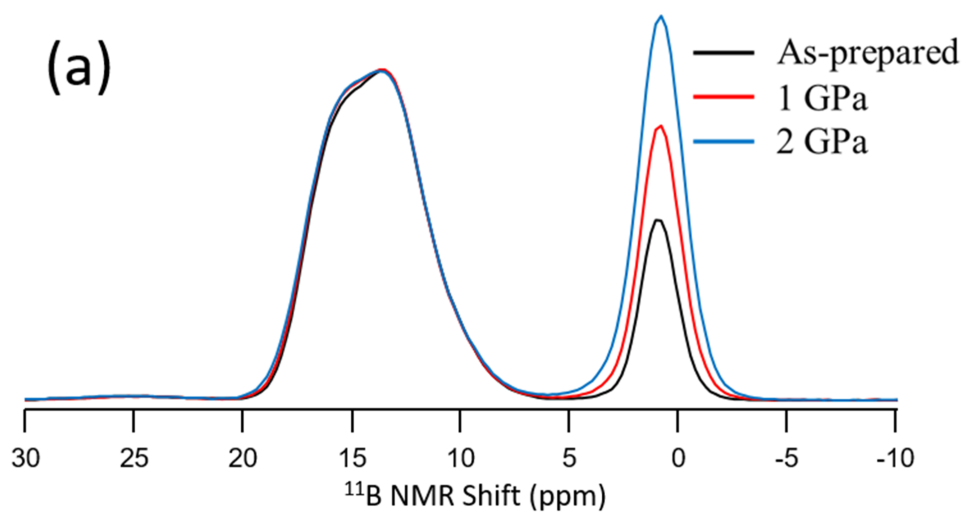


jace\_17559\_f4b.tif

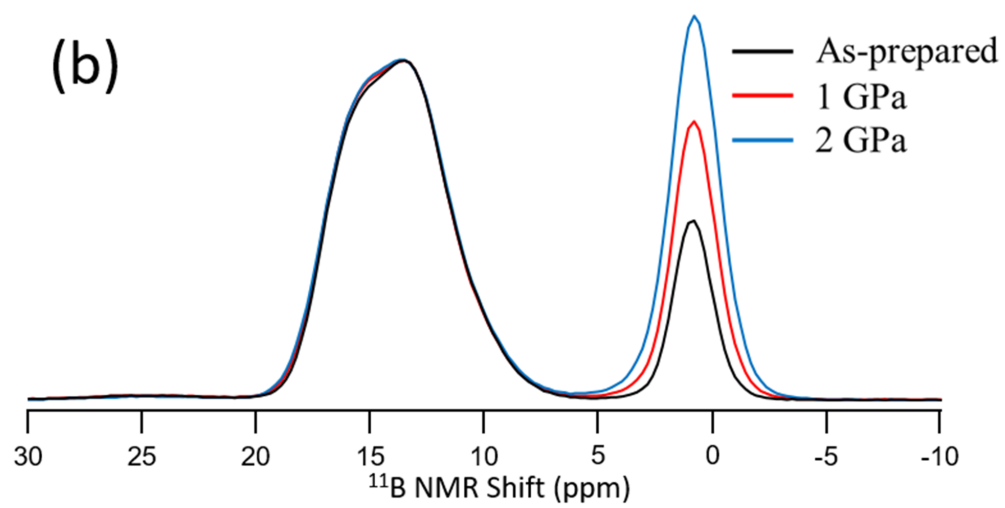


jace\_17559\_f5.tif

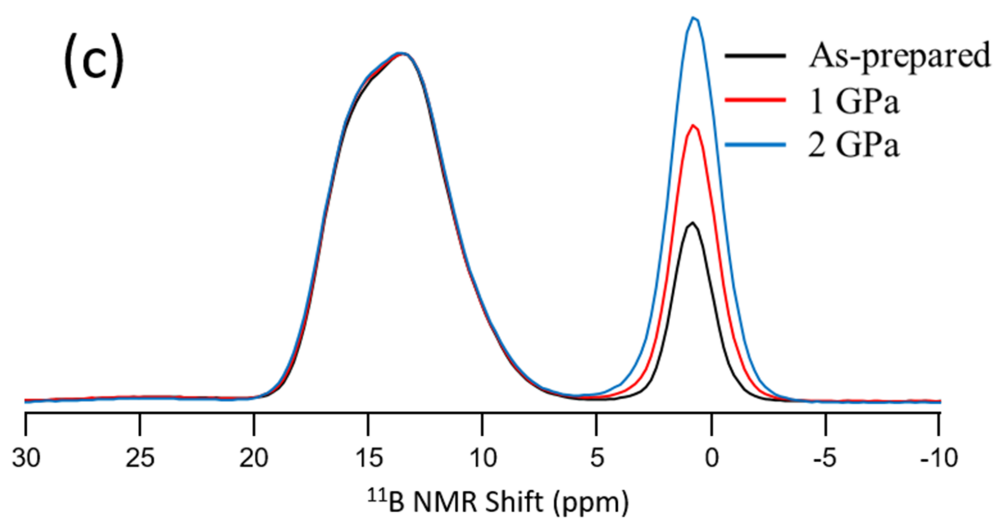




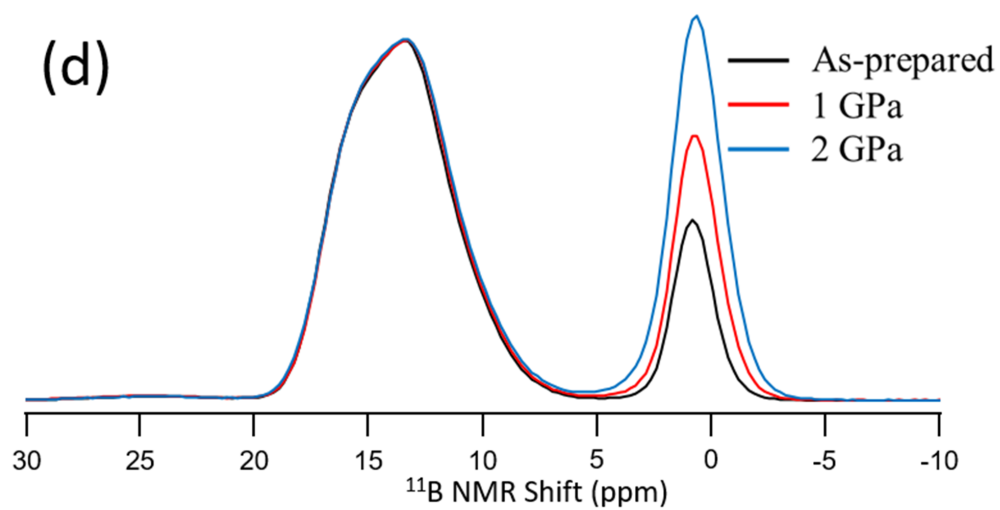
jace\_17559\_f6a.tif



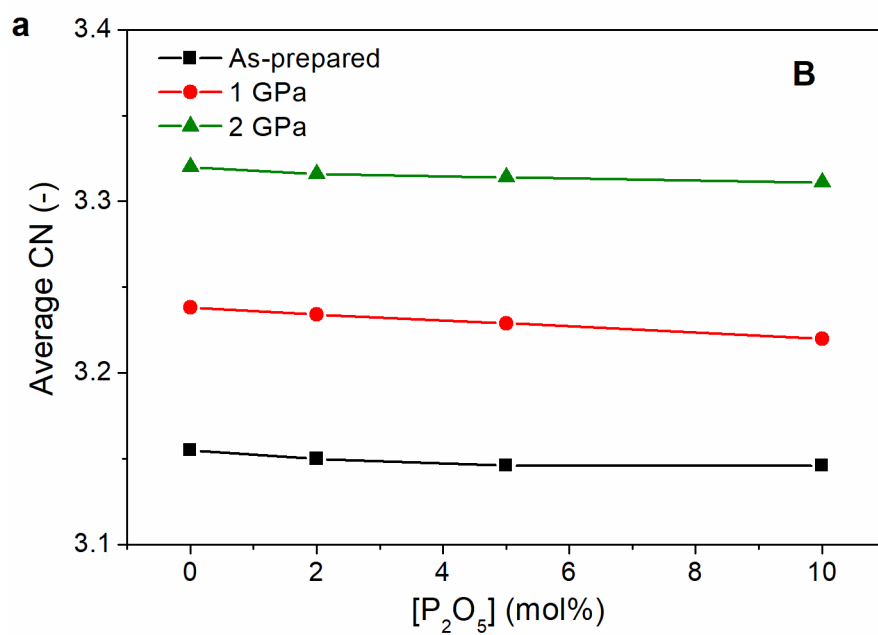
jace\_17559\_f6b.tif



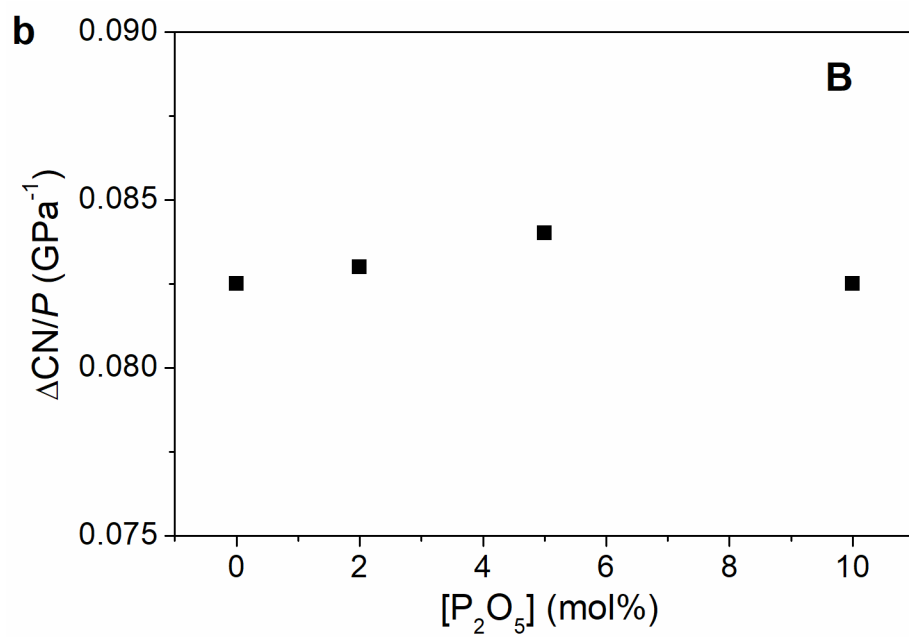
jace\_17559\_f6c.tif



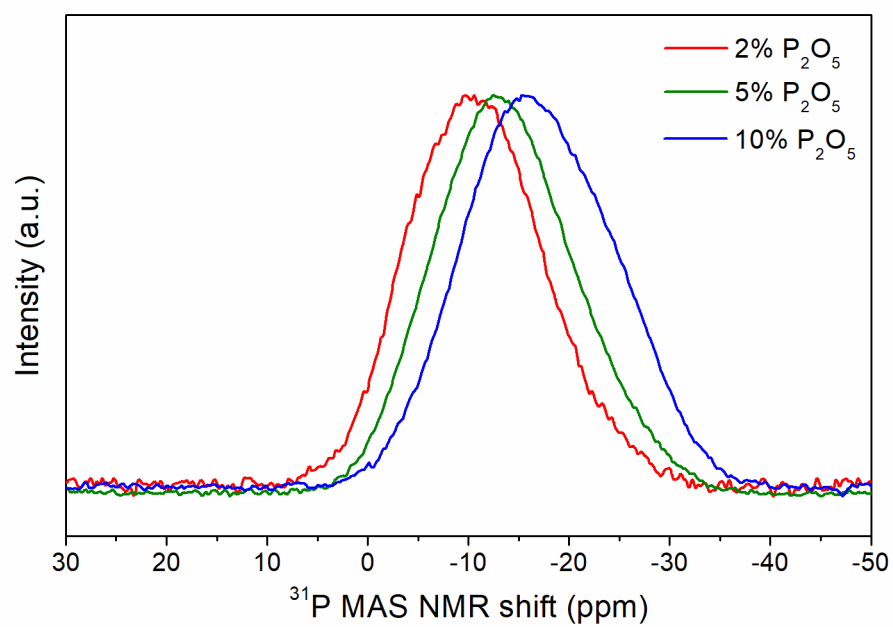
jace\_17559\_f6d.tif



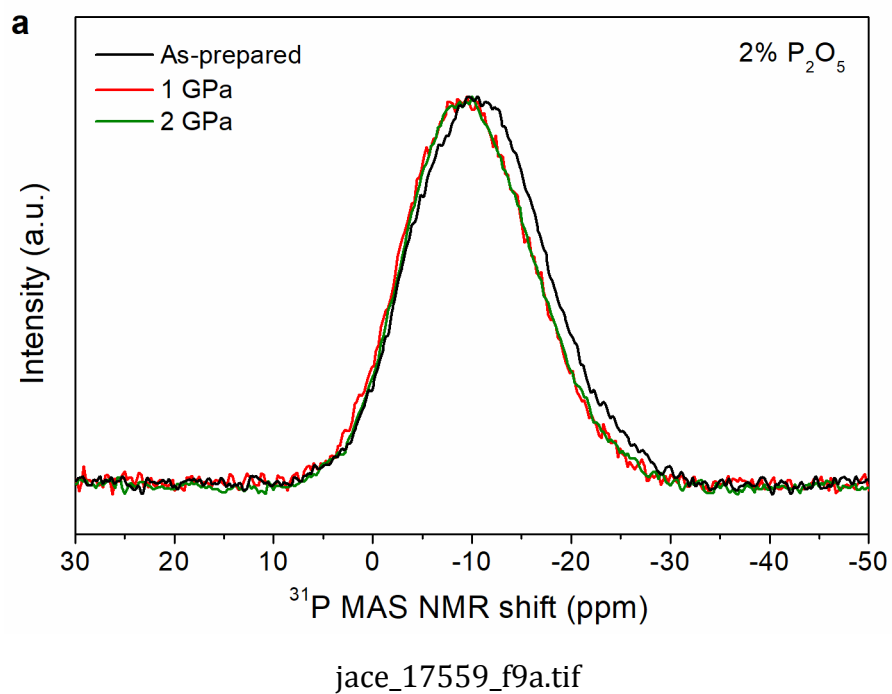
jace\_17559\_f7a.tif



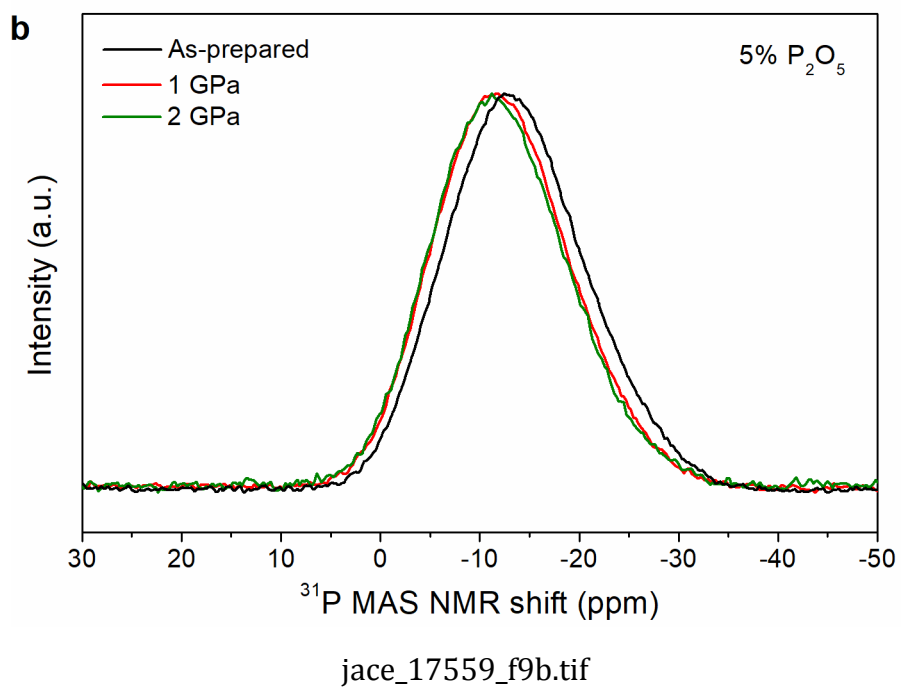
jace\_17559\_f7b.tif

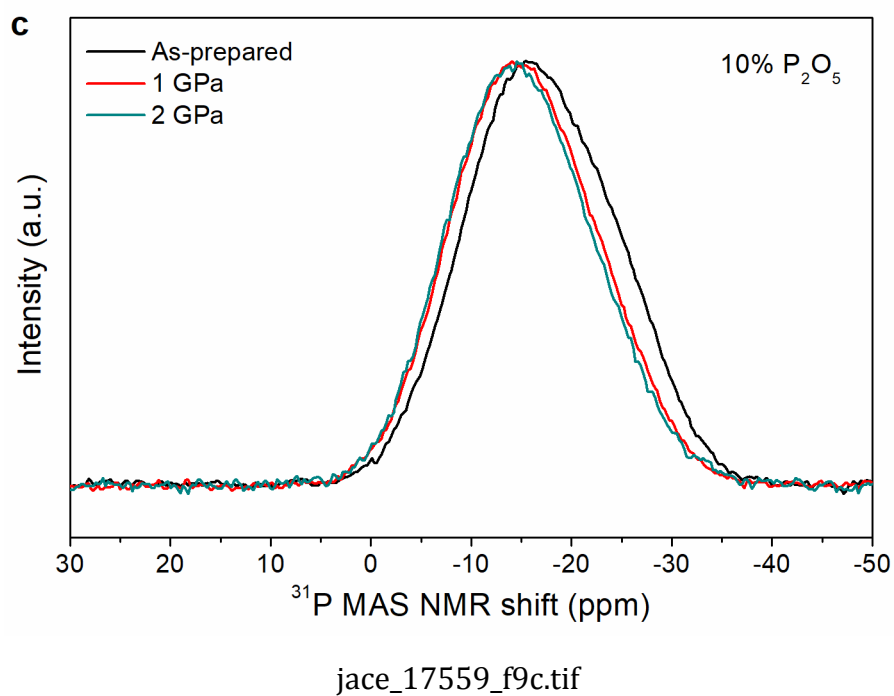


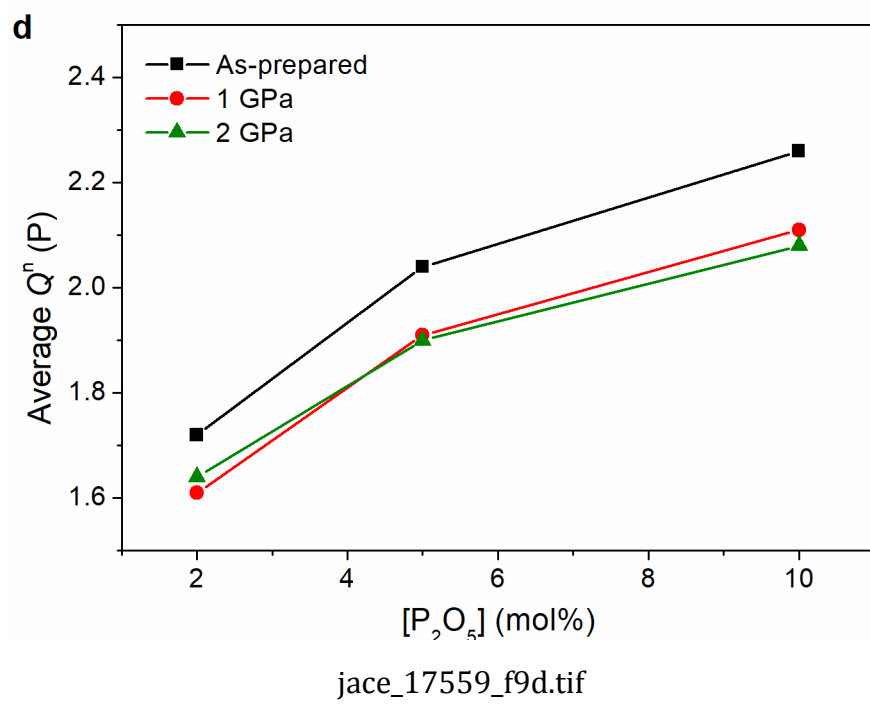
jace\_17559\_f8.tif

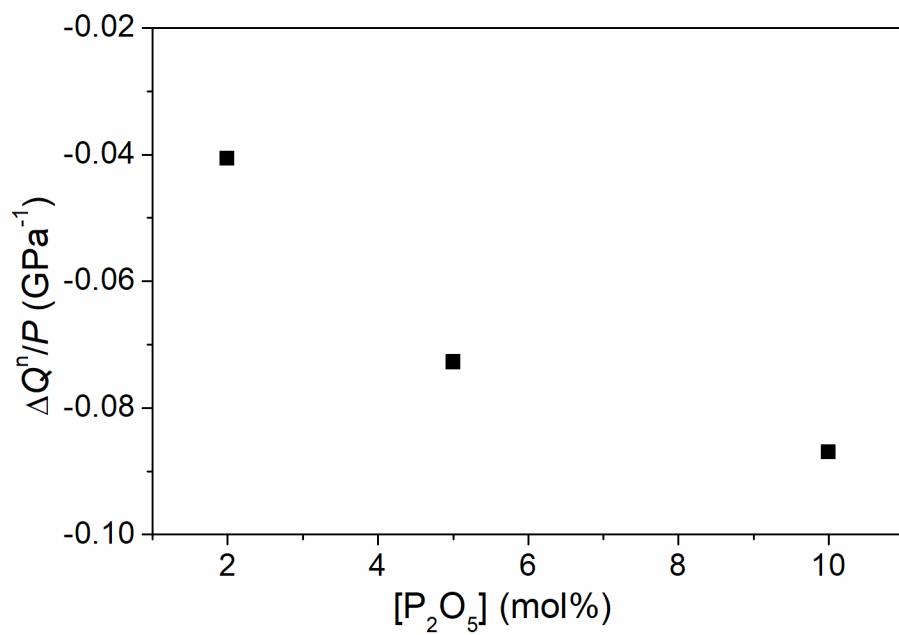




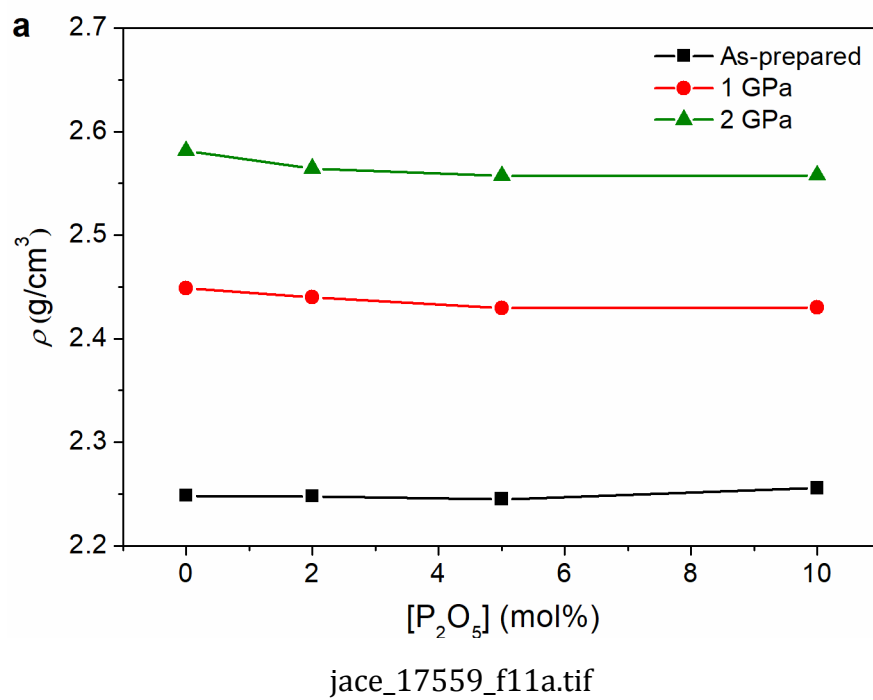


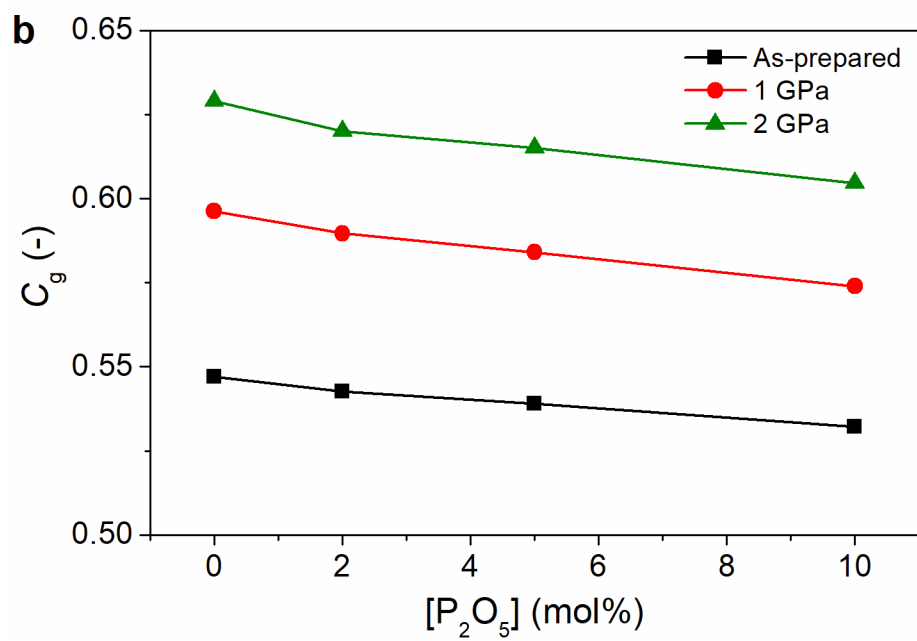




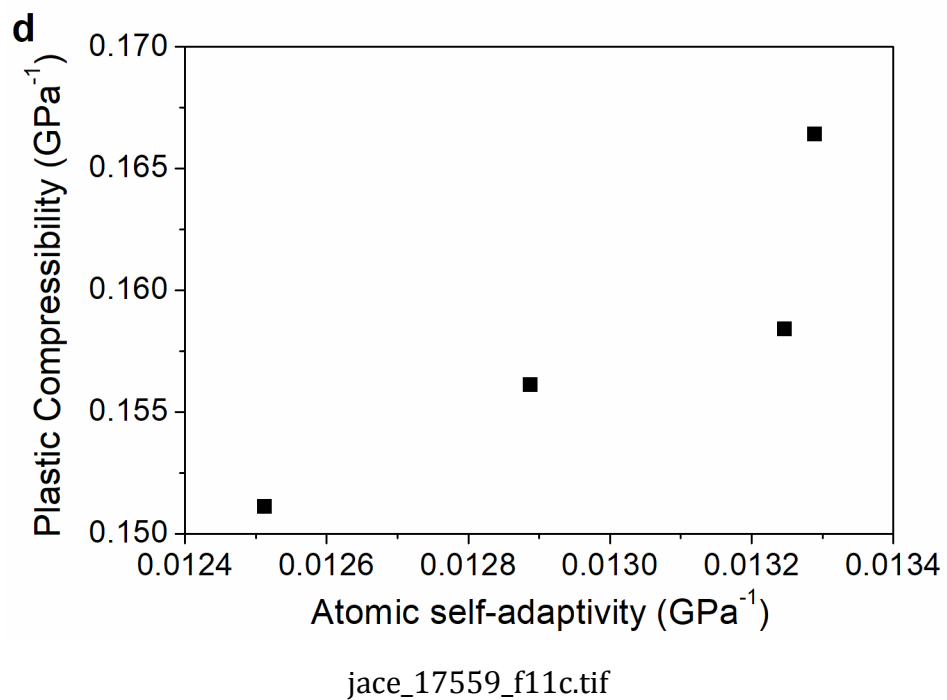


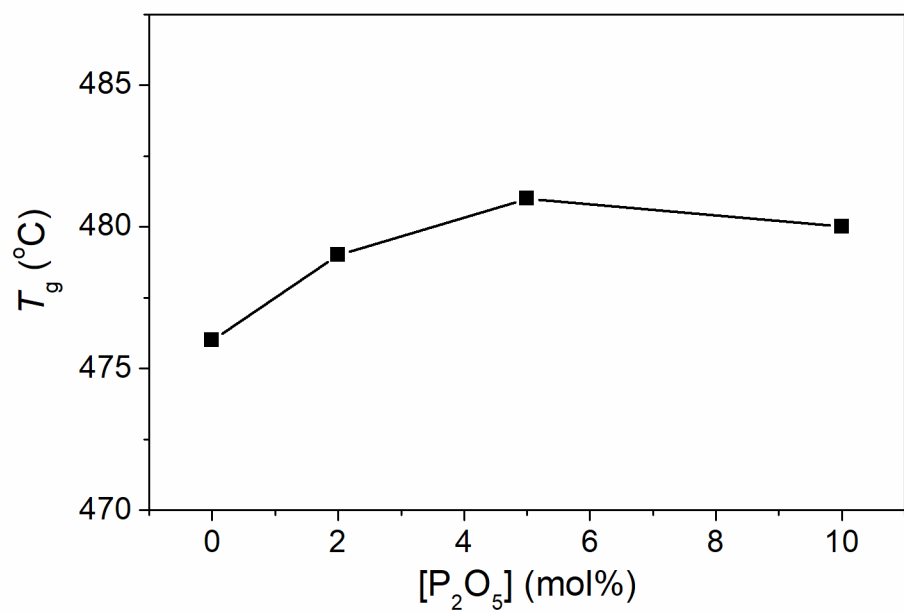
jace\_17559\_f10.tif





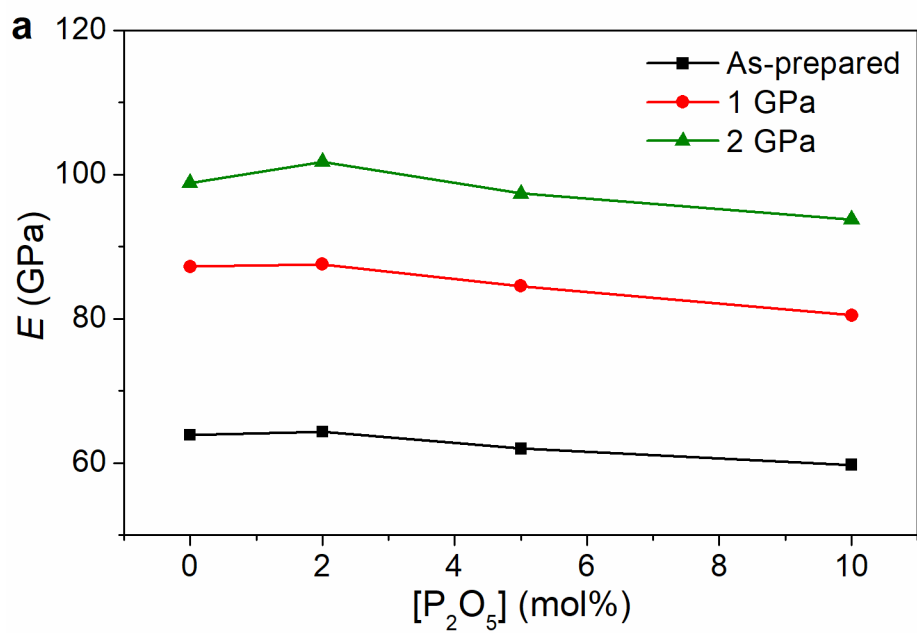
jace\_17559\_f11b.tif



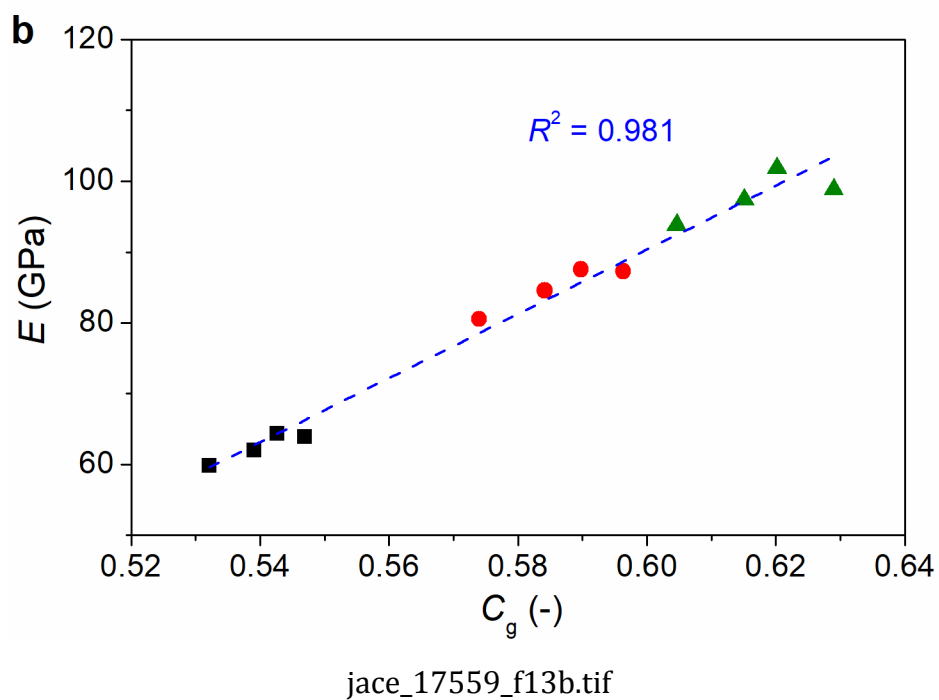


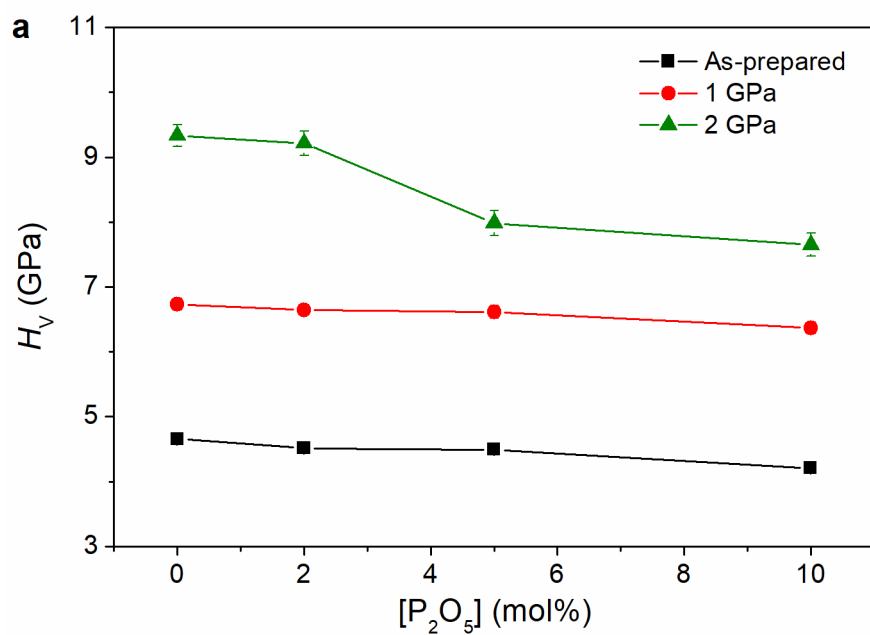
jace\_17559\_f12.tif





jace\_17559\_f13a.tif





jace\_17559\_f14a.tif

